Chapter 3

The Muon Arms Detector Design

In this chapter the details of the Muon Arms design will be presented. It will also cover the current R&D results and construction status of the various components of the detector.

3.1 Muon Magnets

There are two muon magnets in the PHENIX detector. The North Muon Magnet was in the PHENIX baseline. The South Muon Magnet is the result of the upgrade of PHENIX to include a Spin Physics program. Because of constraints imposed by the existing PHENIX detector hall, the South Muon Magnet could not be identical to the North Muon Magnet. This section will describe both of the magnet designs as they currently exist as well as the muon identifier steel which is behind the magnets in each arm [26].

3.1.1 North Muon Magnet

The design criteria for the North Muon Maget was to cover from 1.1 to 2.4 unit of rapidity (10° to 37°), have large acceptance in ϕ for low cross-section measurements, have a p_T kick of 200 Mev/c at 15°, and have an $\int B \bullet dl$ equal to 0.715 Tesla-meter at 15°. Figures derived from Vector Fields magnetic simulation software, shown in Figures 3.1, 3.2 and 3.3, illustrate the potential lines, the flux density in gauss and the saturation in the iron, respectively, for the final design of the North Muon Magnet. Table 3.1 shows $\int B \bullet dl$ integrated from $1.8 < z < 6.29$ m along lines at 15°, 20°, 25° and 30° in θ.

The design for the North Muon Arm magnet has had changed very little since the writing of the PHENIX CDR Update [2]. What changes have been made are the following:

1. The access door at the top of the "teacup" assembly, and its internal ribs have been removed.

2. The depth of the notch in the piston, where the station 2 tracking chambers will be located, is now only be 9.0 cm deep whereas it was defined as 12.0 cm deep.

3. The bolt-on low carbon steel iron plug for the front of the piston has a full radius instead of a sharp corner. It was concluded that the fields at that corner were several
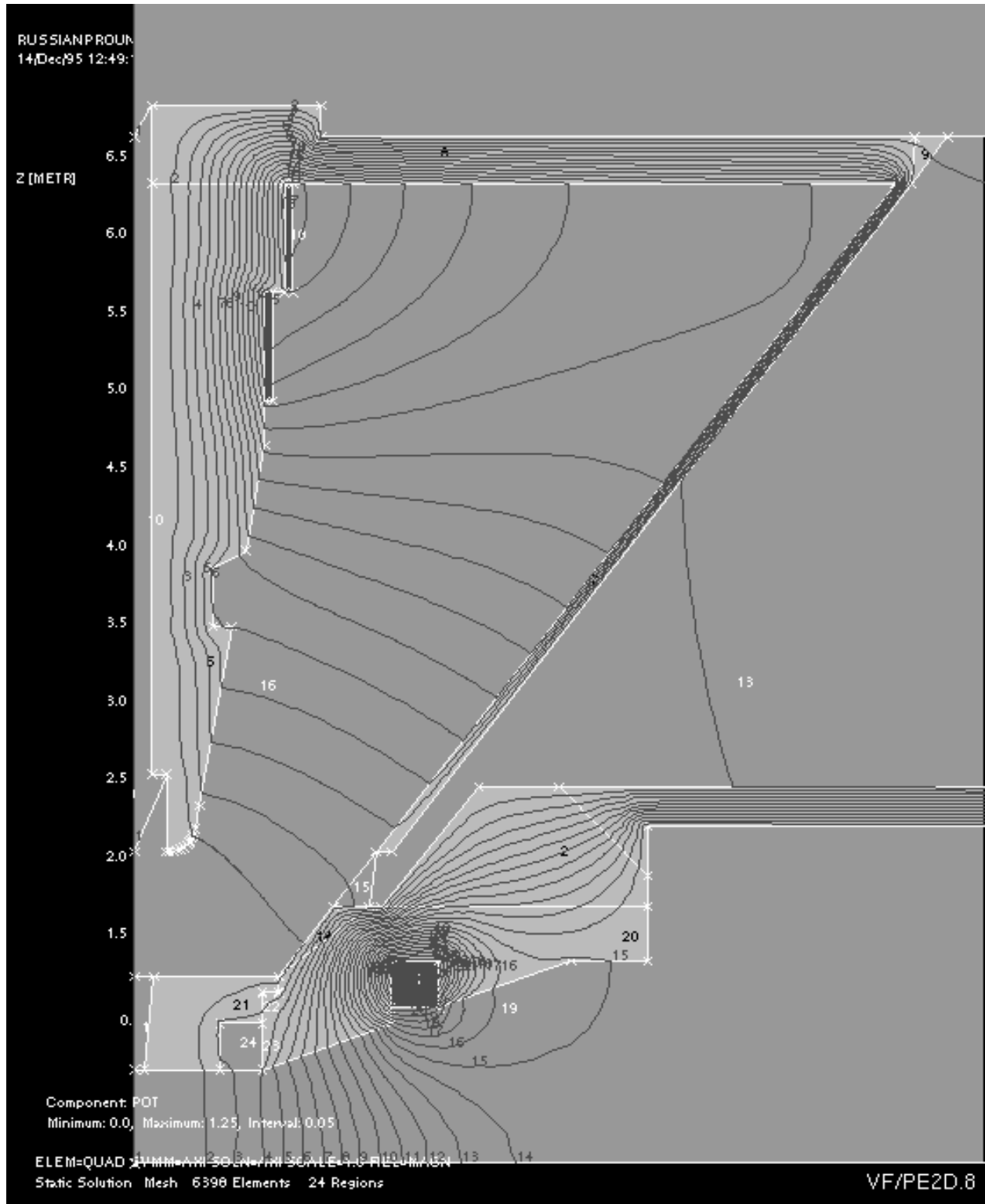
Figure 3.1: A plot of the potential lines of the PHENIX Central Magnet and North Muon Magnet. The radius from the beam axis is shown on the horizontal axis and the distance away from the vertex (z-direction) is shown on the vertical axis. The scale for both axes is meters.

Figure 3.2: Shaded regions on the Central Magnet and North Muon Magnet show the levels of flux density within the magnet volume. The units are gauss.
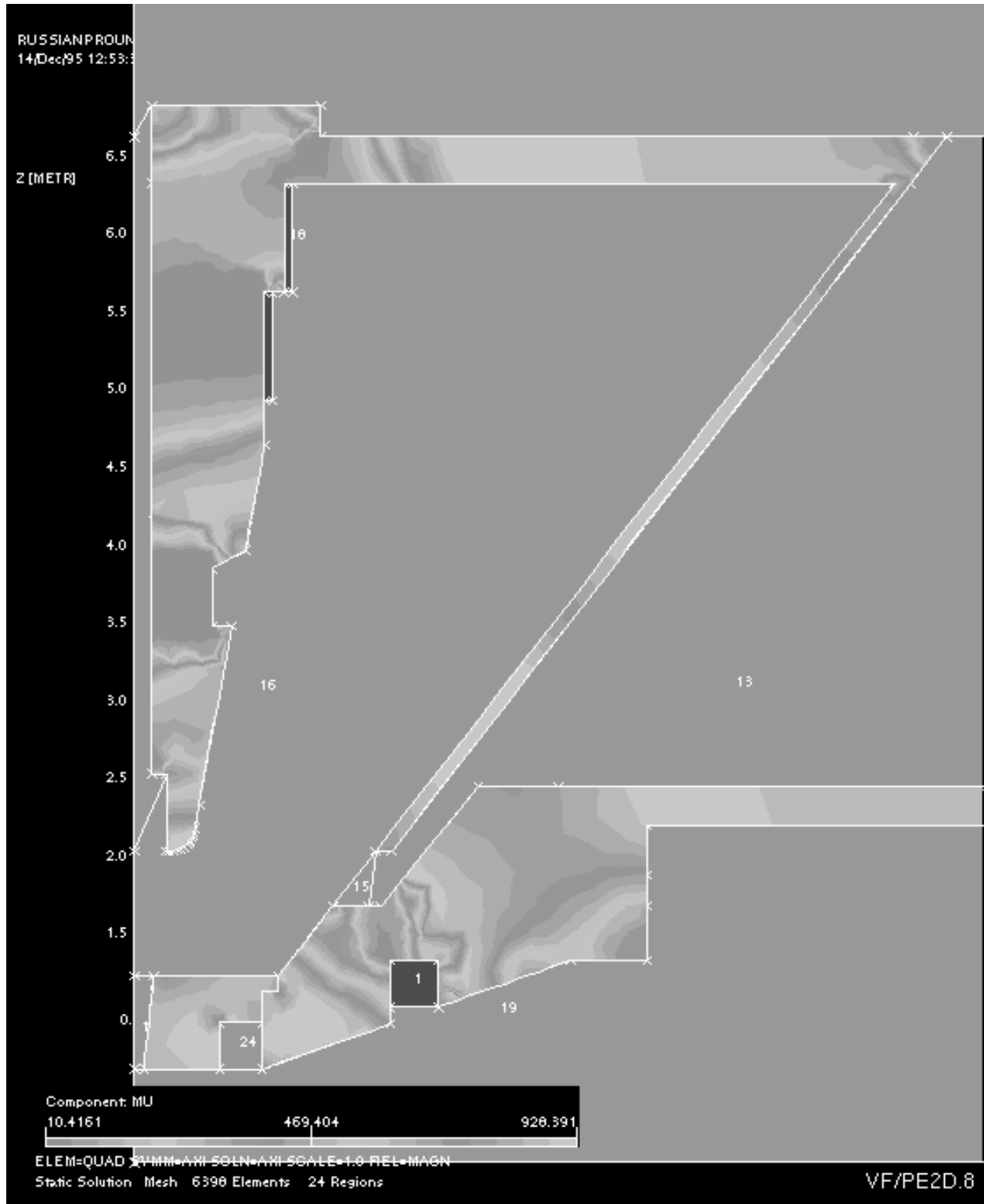
Figure 3.3: The shaded regions on the Central Magnet and North Muon Magnet show the level of saturation of the steel. For example, the North Muon Magnet piston is fully saturated (dark grey) under the smaller diameter coil. The least saturated regions are very light grey.

Angle	$\int B \bullet dl$ (gauss-meters)
15°	7,143.58
20°	4,802.95
25°	3,498.39
30°	2,687.55

Table 3.1: Integration of field valves along a line. The range of z for the integration was from 1.8 m to 6.29 m.

kilogauss, which was too high for the proximity of the station 1 tracking chambers that mount off the front of the magnet.

4. After careful engineering analysis, it was concluded that neither the station 1 nor the station 2 tracking chambers should be mounted from the piston. Instead, they will be mounted from the most stable elements of the magnet assembly, which are the bottom three lampshade panels.

Figure 3.4 shows an isometric view of the Central and North Muon Magnet with the North Muon Identifier absorber plates in place. Figure 3.5 shows a cross-sectional view of both the Central and North Muon Magnet.

3.1.2 South Muon Magnet

In 1995, a Spin physics program was added to the PHENIX baseline. That resulted in the addition of a South Muon Arm to the PHENIX detector. Central to the South Muon Arm is the South Muon Arm Magnet. The conceptual design of that magnet has been given in a muon arm technical note [27] and will only be summarized here.

The design criteria for the South muon magnet are the following:

1. To the maximum extent possible, utilize the existing North Muon Magnet design concept in order to take advantage of the proven design details and subsystem interchangeability.

2. The maximum weight of any single component of the South Muon Magnet should not exceed 40 tons in order to allow the existing PHENIX detector hall crane to be used for the magnet's assemble.

3. Provide Central Magnet accessability by designing for full retraction of the South Muon Magnet up against the South Muon Identifier. That is a distance of approximatelty 1.5 m.

4. Minimize the number of hall track components by following the same design criteria used for the Central Magnet and the central detector arms.
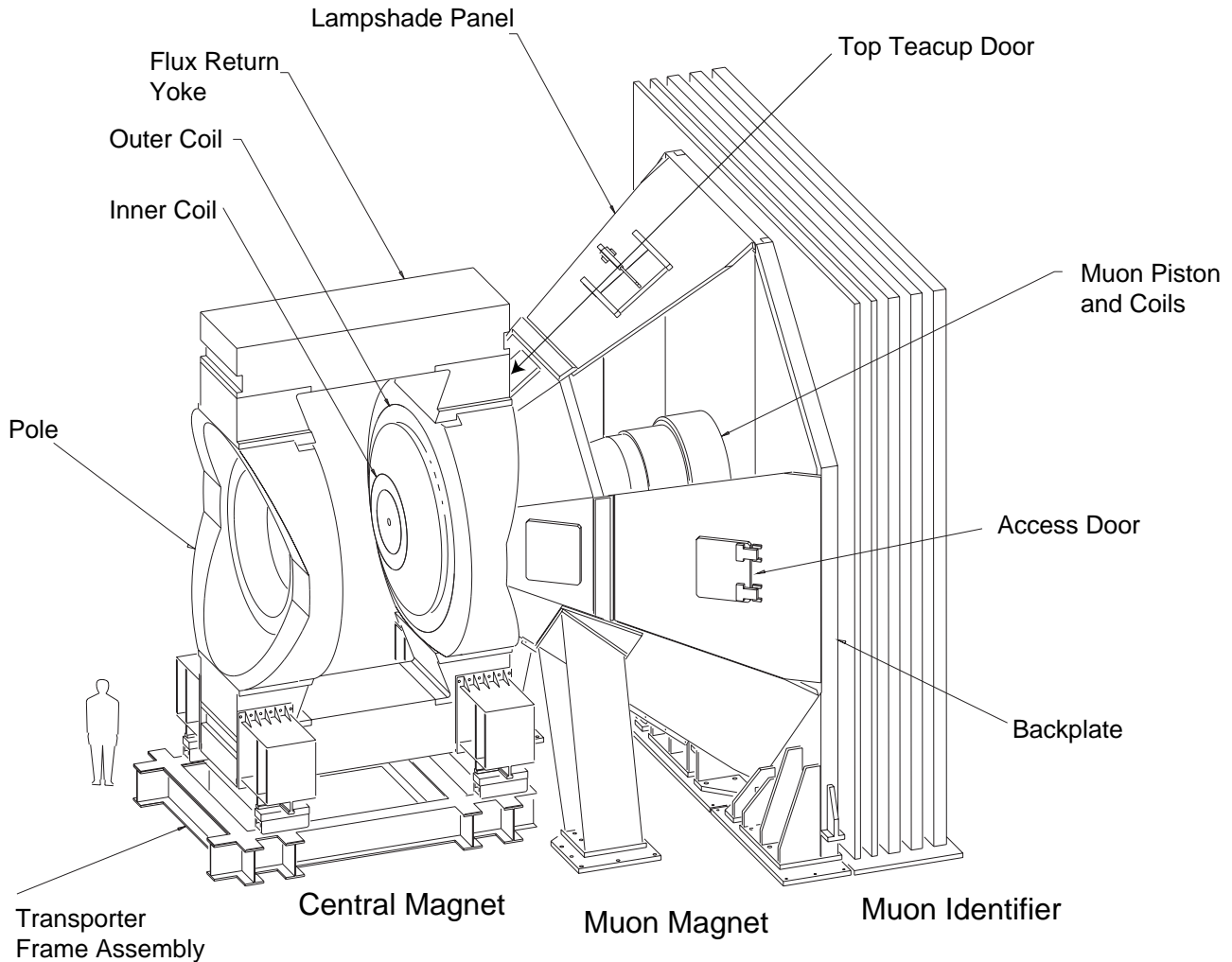
Figure 3.4: Isometric View of the PHENIX Central and North Magnet Subsystems.

5. Try to design for similar a p_T kick of 200 Mev/c at 15°.

The result is a design shown in Figures 3.6 and 3.7.

The two most striking differences between the two magnets is that the South Muon Magnet is 1.5 m shorter, and the piston has to follow a larger angle (12°). This design was developed using Vector Fields magnetic modeling. Figures 3.8, 3.9 and 3.10 show the potential lines, the flux density in gauss, and the saturation of the iron for the final design of the South Muon Magnet. Table 3.2 shows $\int B \bullet dl$ integrated from $1.8 < z < 4.29$ m along lines at 15°, 20°, 25° and 30° in θ.

3.1.3   Tracking Chamber Placement In the Magnets

If one studies the two plots of the potential lines for the two muon magnets (Figures 3.1 and 3.8), it will be noticed that the placement of the second tracking station should not be at

Figure 3.5: Configuration control drawing showing the Central, both Muon Magnets and the Muon Identifier steel in cross-section.

Figure 3.6: Isometric view of the South Muon Magnet

Figure 3.7: Cross-sectional view of Central Magnet and South Muon Magnet.
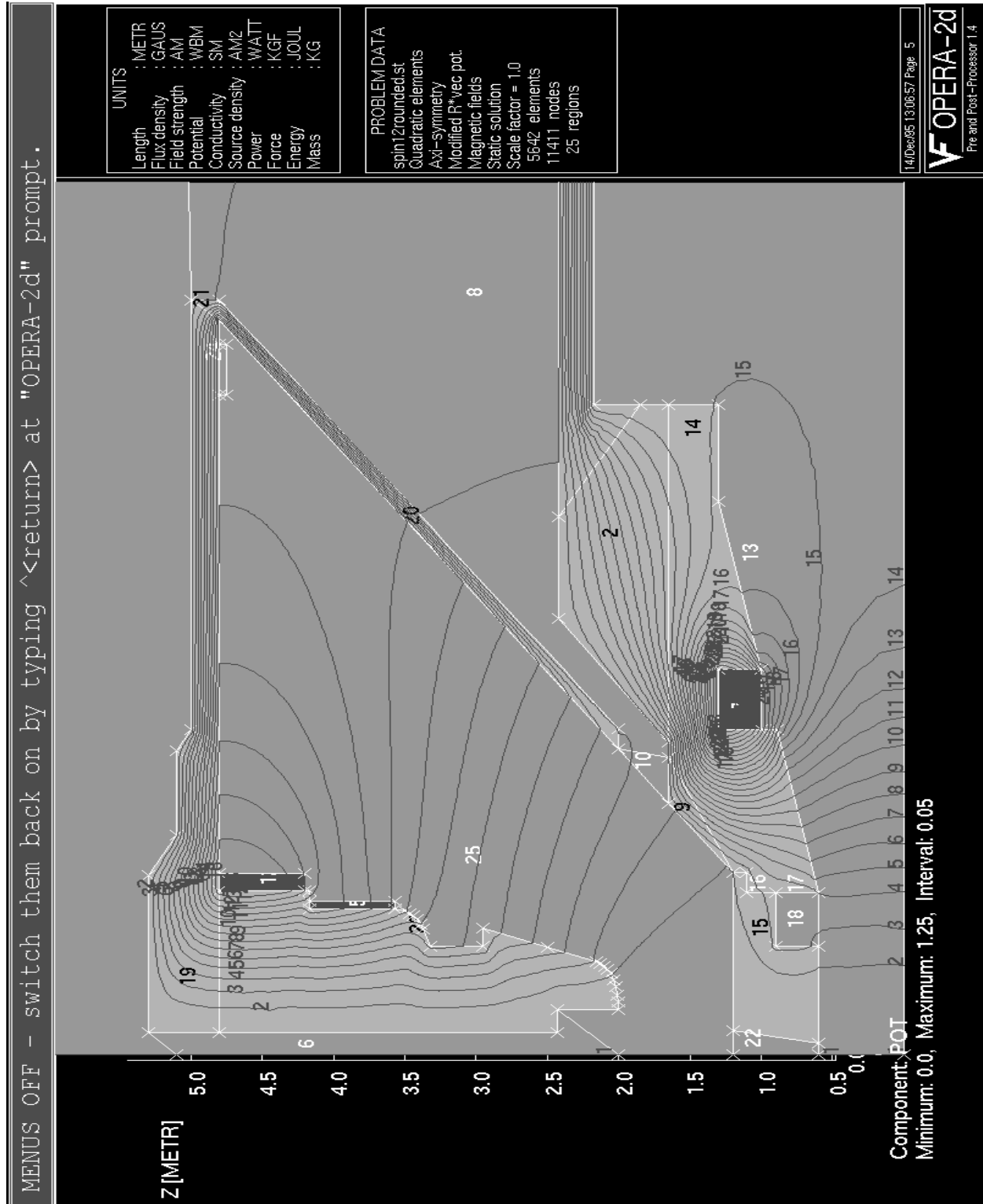
Figure 3.8: A plot of the potential lines of the PHENIX Central Magnet and South Muon Magnet. The radius from the beam axis is shown on the horizontal axis and the distance away from the vertex (z-direction) is shown on the vertical axis. The scale for both axes is meters.
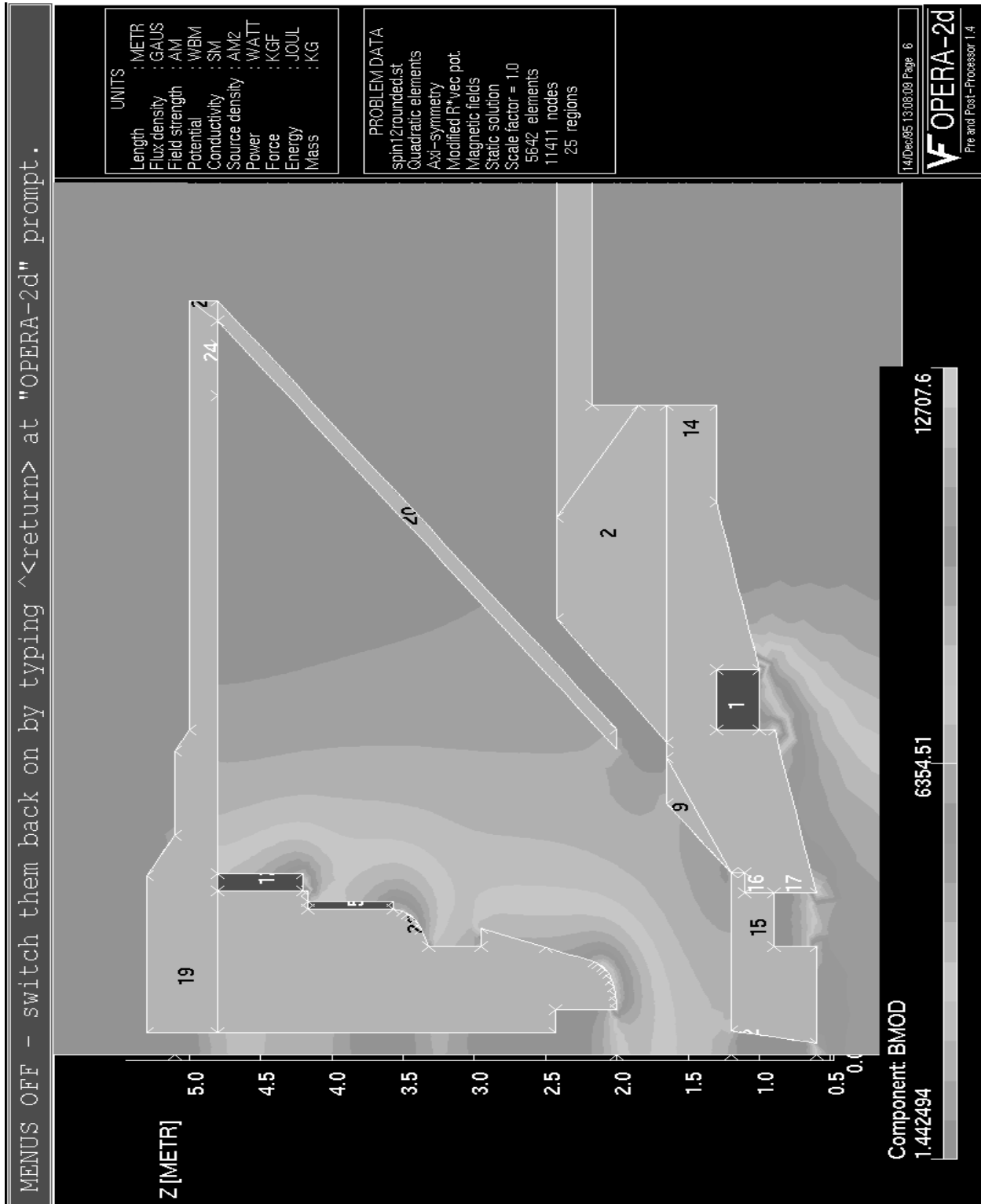
Figure 3.9: Shaded regions on the Central Magnet and South Muon Magnet show the levels of flux density within the magnet volum. The units are gauss.

Figure 3.10: The shaded regions on the Central Magnet and South Muon Magnet show the level of saturation of the steel. For example, the South Muon Magnet piston is fully saturated (dark grey) under the smaller diameter coil. The least saturated regions are very light grey.

Angle	$\int B \bullet dl$ (gauss-meters)
15°	7,679.54
20°	4,931.30
25°	3,447,34
30°	2,557.81

Table 3.2: Integration of field valves along a line. The range of z for the integration was from 1.8 m to 4.29 m.

the mid-point along the length of the piston. To optomize the position of the chambers a careful calculation was done to determine the z-position of the maximum radial deflection of charged particle trajectories in the magnet. The results of these calculations and the z-positions of the chambers for the North and South Muon arms are shown in Figures 3.11 and 3.12.

3.1.4   Muon Identifier Steel

The Muon Identifer Steel which will be used in the detector has been described in detail in the PHENIX CDR Update [2]. In summary, the Muon Identifier Steel consists of five steel plates. The first two are 10 cm thick and the last three are each 20 cm thick. The muon identifier steel for both the North and South Muon Arms are identical.

Since the writing of the CDR Update, the following modifications of the Muon Identifier steel have been made:

1. The muon identifier detector panels are now all of equal thickness. This requires new z locations for the steel absorber rows.

2. The center-plate of the second steel absorber plate is 200 mm narrower than the others. The side plates in this row are the same as in other rows, so the overall width of this row is narrower. This modification helps to hide the cracks in the steel between adjacent plates from row to row.

3. The last muon identifier plate extends under the experimental hall's bridge crane support. Consequently, the last absorber plane is shorter than the others.

The modifications to the North Muon Identifier steel can be seen in Figure 3.5 and are detailed in Phenix Technical Notes [28,29].

3.1.5   Current Status of the Muon Arms Magnets and Identifier Steel

The Central Magnet, both of the Muon Magnets and the Muon Identifier steel for both Muon Arms are now installed in the PHENIX Experimental Hall (PEH). As-built surveys of
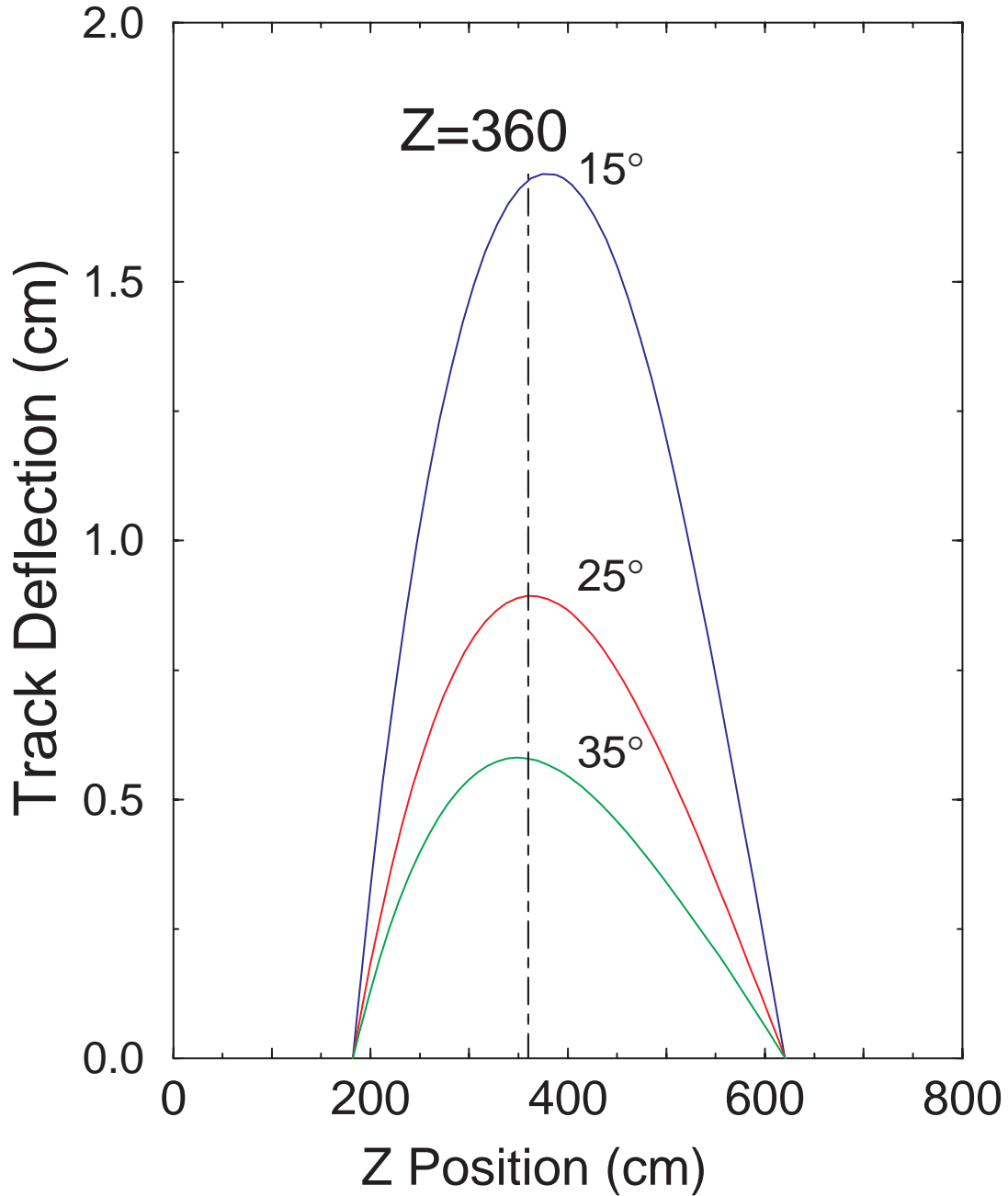
Figure 3.11: The track deflection vs z position for 10 GeV/c μ's in the North Muon Magnet at various θ angles. The optimum position for the Station 2 chambers is shown on each curve.
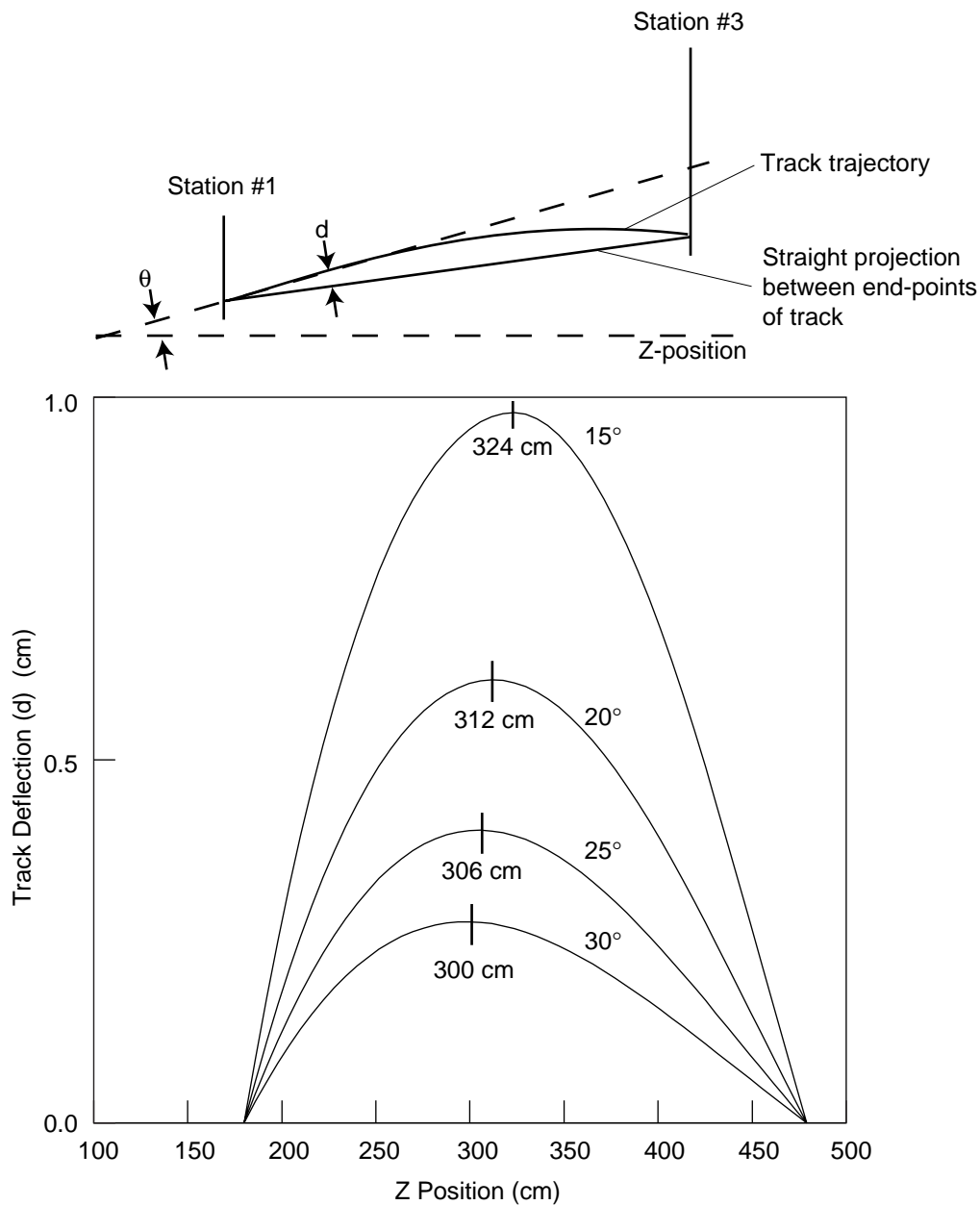
Figure 3.12: The track deflection vs z position for 10 GeV/c μ's in the South Muon Magnet at various θ angles. The optimum position for the Station 2 chambers is shown on each curve.

all three magnets have been performed and have been incorporated into three-dimensional models of the magnets. Those models are an integral part of the final designs for the mechanics of the Muon Tracking chambers and the Muon Tracking Front-End Electronics.

3.2   Absorbers

Several absorbers are a part of the muon spectrometers. These absorbers are continually being developed and are described in some detail in the PHENIX CDR [1], Sections 10.2.2 and 10.4.1, and also in the CDR Update [2], Sections 10.4.2 and 10.6.1. They consist of the copper nose cone, the copper insert (or flowerpot) and the iron plug. The lead curtain and neutron absorbers have been removed from the designs since they were shown not to be needed for background reduction and would actually led to somewhat reduced dimuon mass resolution. The absorbers for the North Muon Arm are all shown in Figure 3.13. There is a similar set for the South Muon Arm.

The copper nose cone is bolted on the central magnet pole tips. The purpose of the nose cones are to reduce the flight path for hadrons from the collision point to the hadron absorbers (starting with the central magnet pole pieces). This results in a decrease in the number of muons from weak decays that enter the muon arms. The final nose cone designs are now in progress. Past designs showed them to be assymmetric with the one in front of the South Muon Arm being thinner. It has recently been decided that they will be the same thickness for both arms.

The copper insert, or flowerpot, is attached to the downstream sides of the central magnet pole pieces. The inserts serve two primary purposes. First, they are the mounts for the beam-beam counters, and second, they stop particles from shower leakage out of the central magnet pole piece from entering the tracking chambers. Additionally, they provide more absorber material for the more energetic primary particles at very forward angles which would strike the front face of the piston. The inserts have an outer tapered edge following the 10° and 12° lines matching the muon magnet piston angles for the North and South arms, respectively. They are both bored out to accomodate the beam-beam counter on each side of the vertex. Currently shielding studies are under way to optimize the design of these absorbers.

The last absorber is the iron plug. It is the front part of the muon magnet piston. Each is bored out to almost twice the diameter of the piston bore so that particles will not shower off the front of the piston into the first tracking station. This larger bore is also necessary to provide space for a flange in the beam pipe that will be in this region.
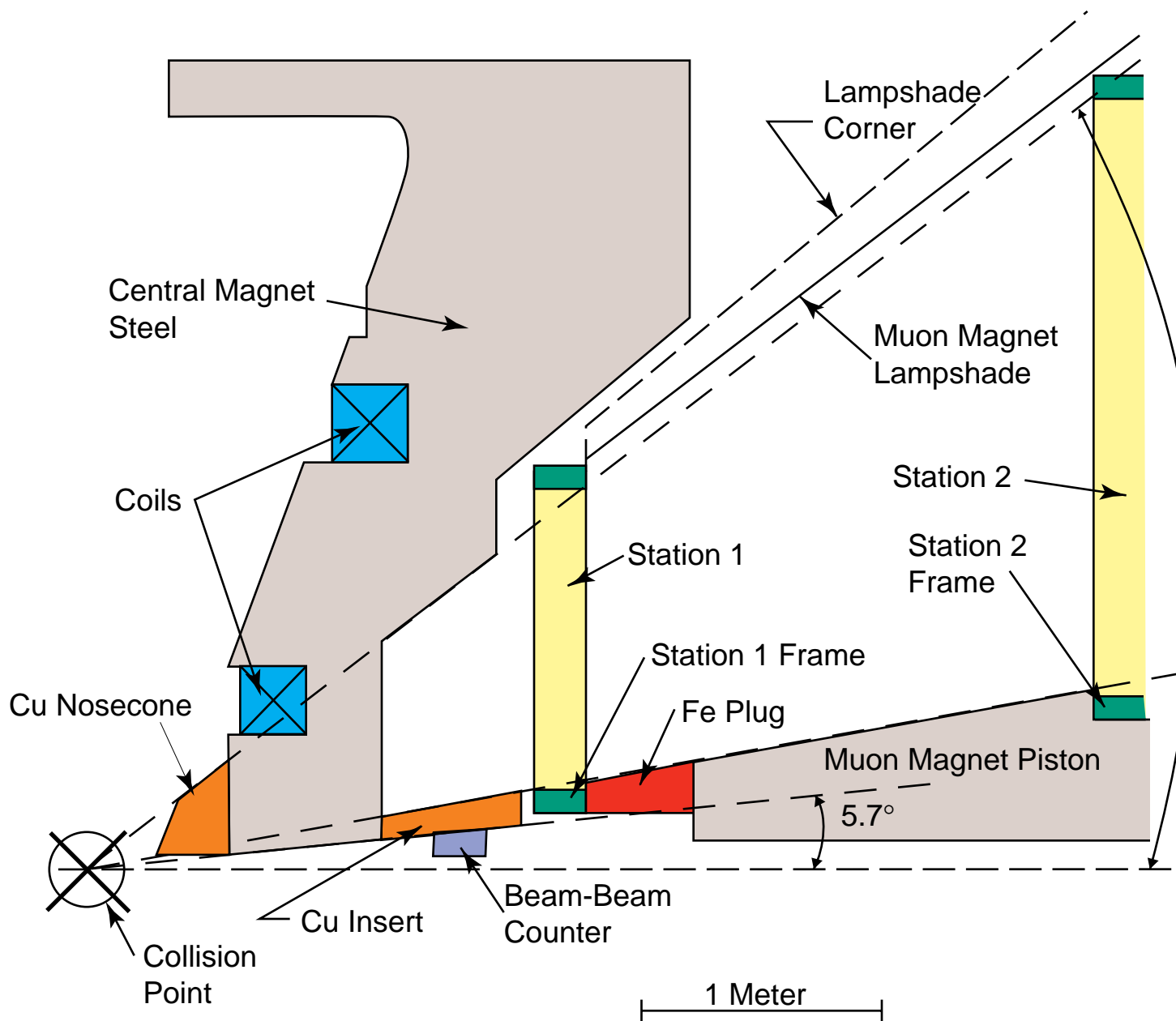
Figure 3.13: A view of the North Muon Arm showing the layout of the specialized absorbers. The absorbers for the South Muon Arm are essentially a mirror image of these with the exception that they follow a 12° outer angle to match the South Arm pistion.

3.3   Tracking Chambers

This section describes the kind of chambers which will be used for muon tracking in the Muon Arms spectrometer. It then presents the design details for the chambers and some information on how they will be manufactured. Finally, some R&D results on various prototype chambers is presented.

3.3.1   Introduction to Cathode Strip chambers

The basic mechanical construction of the cathode strip chamber CSC is that of a conventional proportional wire chamber. However, rather than reading out the anode wire to get discreet position resolution, a precise position coordinate is determined from the induced signal on cathode strips perpendicular to the anode wires. Resolutions as small as 50 μm have been achieved on chambers as large as 2 m [30]. For the CSC to serve as the muon system tracking chambers, several issues were addressed. These include spatial resolution, identification of a suitable gas with a small Lorentz angle, radiation length, preparation and metrology of the cathode foils, and mechanical design issues related to frame stiffness, frame thickness, and creep. Cost and simplicity in design were additional factors.

CSC signals

The charge on the anode is due to ionization in the gas caused by passage of the muon through the gas volume and the gain of the chambers. In a typical gas volume the ionization process produces about 140 electrons/cm so in the CSC chambers the number of electrons produced will be 140×0.7 cm electrons or 100 electrons per track. Assuming a gain in the chamber of 2×10^4, the anode charge will be 2×10^6 electrons. The cathode charge is one half of the anode charge times a reduction factor called the "ballistic deficit factor" that is due to the finite integration times. Taking a ballistic deficit factor of 0.5, the total cathode charge will be 5×10^5 electrons, or 80 fC.

Cathode Strip Chamber Design Issues

The primary design issues addressed have been factors effecting the intrinsic resolution of the chambers, the mechanical and electronic requirements, and the definition of a suitable gas. Where possible we have relied on the work of previous authors and in particular the vast amount of work done by the Muon Group and the Central Tracker Group of the former GEM collaboration at the SSC.

CSC Candidate Gases

It is desirable to have a gas with a small Lorentz angle so resolution degradation due to a large Lorentz angle can be minimized. Fortunately, a number of fast gases have been identified and tested that are suitable for the CSC's. Most of these gases contain CF_4 in combination with isobutane or CO_2. The Lorentz angle is similar for each gas and is about
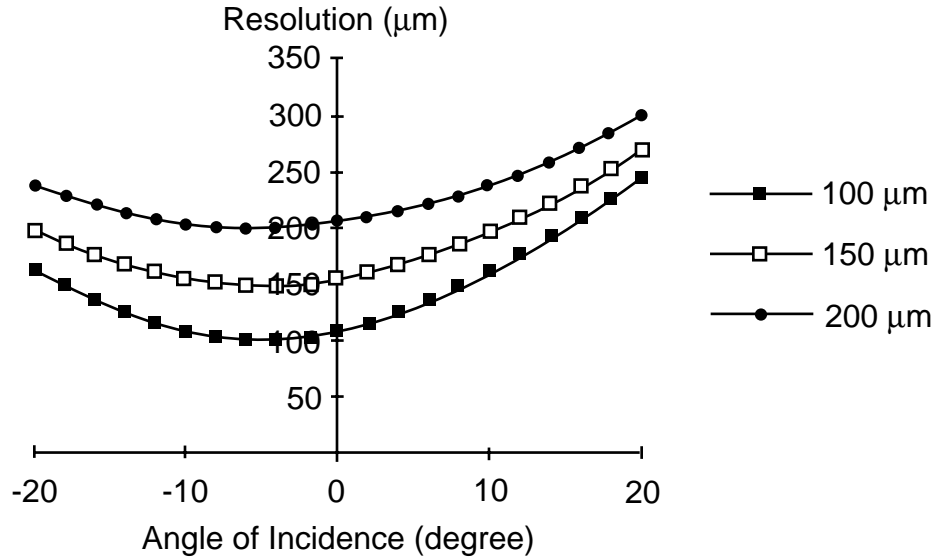
Figure 3.14: Resolution degradation as a function of incident angle for different intrinsic resolutions in CSC chambers.

5° at 0.5 Tesla magnetic field. Most of the prototype work has been done with a 50% CF_4, 50% isobutane mixture.

Resolution Degradation Due to Inclined Tracks and Lorentz Angle

Resolution degradation of the CSC's comes primarily from two causes–tracks inclined from the normal to the face of the chamber and Lorentz angle. In both cases, the position resolution is degraded because the deposited charge is distributed nonuniformly along the anode wire due to the energy loss fluctuations in the gas. These effects have been extensively studied by the former Muon Group in the GEM collaboration and reported in a GEM note [31]. Additional studies by Musser, *et al.* [32] for the GEM Central Tracker Group on a CSC type chamber very similar to the proposed PHENIX CSC's and for a suitable gas (50% CO_2,50% CF_4) have shown that the resolution degradation, d, is equal to

$$d = 0.08l \tan \phi \tag{3.1}$$

where l is the cathode to cathode spacing and ϕ is the angle from the normal to the face of the chamber. Including Lorentz angle smearing is accomplished by modifying the angle of incidence by the Lorentz angle, φ, i.e. ϕ-φ. In Figure 3.14 and Figure 3.15, we show the chamber resolutions when these effects are taken into account. The Lorentz angle was taken to be 5°. In Figure 3.14 the resolution is plotted for chambers with different intrinsic resolutions and the chamber gap = 6 mm. In Figure 3.15 the resolution is plotted for different chamber gaps with the resolutions fixed at 100 μm. It is clear that we want thin chambers and small angles of incidence and resolutions approaching 100 μm.
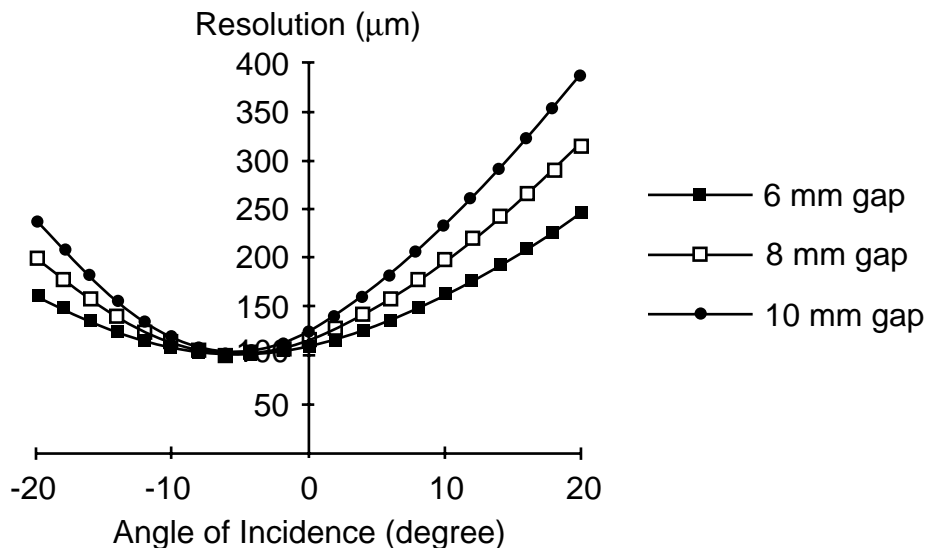
Figure 3.15: Resolution for different chamber gaps at 100 μm intrinsic resolution.

3.3.2   Cathode Strip Chambers Design Constraints

The simulation studies have shown that the mass resolution of the Υ continually increases with the resolution at each station until it is limited by the multiple scattering due to the absorber in front of the muon spectrometer. An Υ mass resolution approaching 200 MeV is achieved if the station resolution is 60 μm. This can be achieved with 3 planes of CSC's with 100 μm resolution at each station. More detailed studies of the design have shown that having only two planes at the third tracking station in our spectrometer does not significantly degrade the resolution. Consequently, our baseline design will read out three planes at Stations 1 and 2 and only two planes at Station 3. (Mechanically, the third plane will be present in Station 3, but due to budgetary constraints it will not be instrumented.) Achieving 100 μm resolution for each plane of CSC's requires careful attention to the design of the cathode strips, the geometry of the drift cell, and signal-to-noise. Generally the dominant factor contributing to the resolution is the electronic noise.

An important aspect to the design of the individual stations is to insure that the detection efficiency is maintained in the face of failure scenarios. The simulation studies have shown that sufficient redundancy exists with three CSC detectors per station to insure 99% tracking efficiency. We have baselined three CSC detectors per station with three coordinate readout for each detector for a total of 9 measurements per station at Stations 1 and 2 and 6 at Station 3. Each detector will read out two high resolution cathodes and the anodes. By reading out both cathodes and the anodes in each detector complete space point reconstruction is possible for each detector without ghost hit interference. Such a robust system simplifies pattern recognition and maintains high tracking efficiency in the event of failure.

The cathodes will incorporate the floating strip method to reduce the number of analog readout channels. Each strip will be 5 mm wide with the readout at 1 cm intervals. With this scheme we expect resolutions of less than 100 μm. The floating strip will be tied to ground

through a 500 kohm resister. The six cathodes in each station are oriented perpendicular to the wires and at either $-11.25°$ or $11.25°$ with respect to the radial coordinate.

The anode plane will incorporate a standard digital readout scheme with an alternating signal/field wire structure to enhance chamber stability. The anode wires are read out on a 5 mm spacing radially. Provision is being made to allow the lowest radius wires at Station 1 to be turned off if the occupancy for that set of chambers presents a problem. All anode planes in a station will have the same orientation.

3.3.3   Stations 1 and 3 Designs

We have incorporated honeycomb structures as the baseline design for the CSC chambers at stations 1 and 3. Several reasons led us to decide on the use of honeycomb structures. Since the radiation length budget ($<10\%$) for stations 1 and 3 is less restrictive than for station 2 ($<0.5\%$), we were not under the restrictions of having to use thin foils for the cathode structures. Honeycomb allows us to have chamber designs which have a larger acceptance than if metal frames were used. The cathodes can be made out of etched copper clad in a commercial process that reduces the manpower required and offers a less expensive chamber design than with foils.

3.3.4   Station 1

The station 1 design is shown in Figure 3.16. Station 1 chambers are designed to be quadrants mechanically but octants electrically. The design calls for four honeycomb structures to form three CSC chamber gaps. The total combined thickness is less than 10 cm. A crossection of the assembly is shown in Figure 3.17. The pair of cathode surfaces on either side of the chamber gaps have cathode strips etched in copper clad epoxy fiberglass skins. The anodes follow the chord in each $22.5°$ segment to minimize effects due to the Lorentz angle of the gas. The anodes span octants only and are electrically isolated at $45°$.

The support frame for the honeycomb panels are 1.8 cm thick by 2 cm wide lucite on the quadrant radial edges and are part of the inactive area of the chambers. The frame support at the inner radius is inside of $10°$ and the frame support on the outer radius is outside of $35°$. At $45°$, the anode support structure and central honeycomb support structure is 1.5 cm wide. This quadrant design maximizes the active area of the chambers.

Mechanical Assembly

We are prototyping two methods for manufacture of the honeycomb structures, a commercial manufacturing process and an "in-house" manufacturing process. The constraints are that the flatness of the panels must be less than 150 μm. The advantages of the commercial process is less local manpower but at a higher material cost. In the "in house" method, the cost will be less but more manpower will be required. In both processes, the outer skins will be bare epoxy fiberglass, 250 μm thick. Precision made and drilled etched cathode skins will be laminated to the panels in a subsequent process utilizing precision machined guide plates. The laminations for both will be done locally to control assembly tolerances. The etched
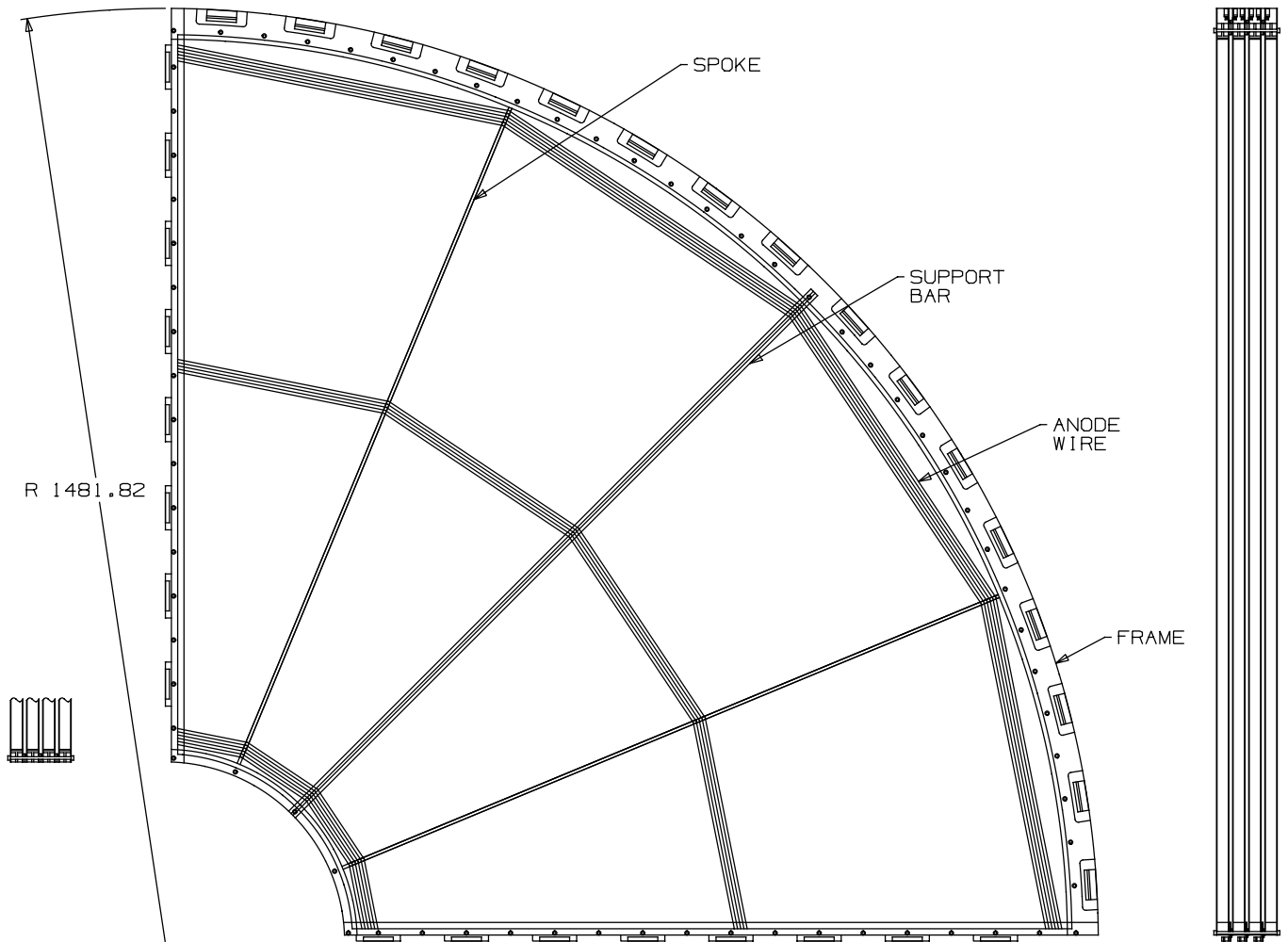
Figure 3.16: Station 1 Quadrant.

cathodes will have alignment fiducials as part of the art work. The goal of the assembly process will be to control the position of the etched cathodes with respect to the alignment pins to better than 25 μm. The gap between panels will be controlled by the anode support structure and the edges of the quadrant and by the support structure at 45°. 50 μm tolerance at these locations is expected. The maximum unsupported anode wire length is less than 58 cm. An anode PC board is used on the edges of the quadrants to distribute the HV and to transmit the signals to IDC connectors. Surface mount components will be used for the capacitors and resistors and all components will be external to the active area. The PC board will extend beyond the edge of the quadrant by 1.5 cm. The anode wires will be held to the PC board by glue and solder and the positioning of the anode and field wires will be determined by fixturing. The anode supports at 22.5°, 45°, and 67.5° are delrin plastic with precision grooves. At 45° the wires will be glued and soldered while at 22.5° and 67.5° the
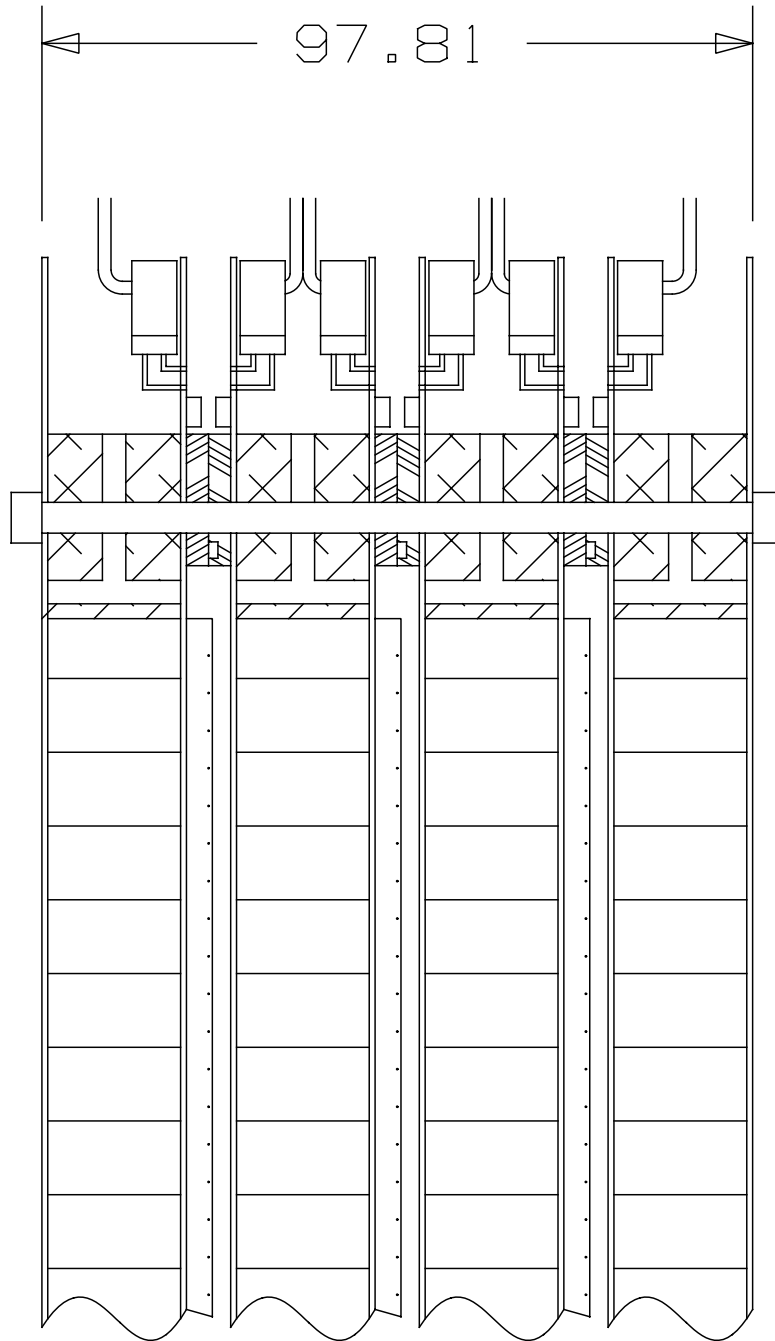
Figure 3.17: Station 1 Quadrant Cross Sectional View.

Component	density	cm/X0	total X0
Hexcel	0.14	485.7	0.0148
Epoxy Fiberglass	1.7	19.4	0.0325
1/2 oz copper	8.96	1.43	0.0095
frames	1.2	34.4	0.209

Table 3.3: Radiation Length of the Materials in the CSC Module.

wires will be glued.

Radiation Lengths

The radiation length of the materials in the CSC module is shown in Table 3.3. Each module is considered to be an active volume surrounded by frames that are inactive for detecting muons.

The total radiation length for the active area of the station 1 module is 5.7%, well within our budget. The frames at the octant boundaries are 20.9% from the lucite and 14.4% from the epoxy fiberglass for a total of 35.3% radiation length.

3.3.5   Station 3

The design for station 3 will be very similar to station 1 except that mechanically and electrically it will be in the shape of an octant. Additional support structure will be added to insure that the mechanical vibrations are kept below 25 μm. A preliminary design is shown in Figure 3.18. The support in the middle of the chamber following a chord covers the same angular range as the support member for station 2. The cross section of the chamber is the same as station 1 and the radiation length thickness is 5.7%. All other aspects of the station 3 design is identical to station 1.

3.3.6   Station 2 Design

The station 2 chamber design is the most ambitious because of the severe radiation length restrictions. Foil cathode structures without honeycomb were required. In addition, to keep the acceptance as high as possible, the frame material surrounding the active area was kept to a miminum. We were able to minimize the frame material by overlapping the adjacent octants, a possibility for the CSC chambers because the active thickness of the CSC's were very small at 3 cm.

Station 2 design criteria

The station 2 assembly is shown in Figure 3.19. Each octant is a separate module that is tied together by a support structure that fastens all eight octants rigidly to the magnet. The octant designs are shown in Figure 3.20 and the cross section is shown in Figure 3.21. The module consists of thin frames for the cathode foils and wire planes stacked in a sandwich
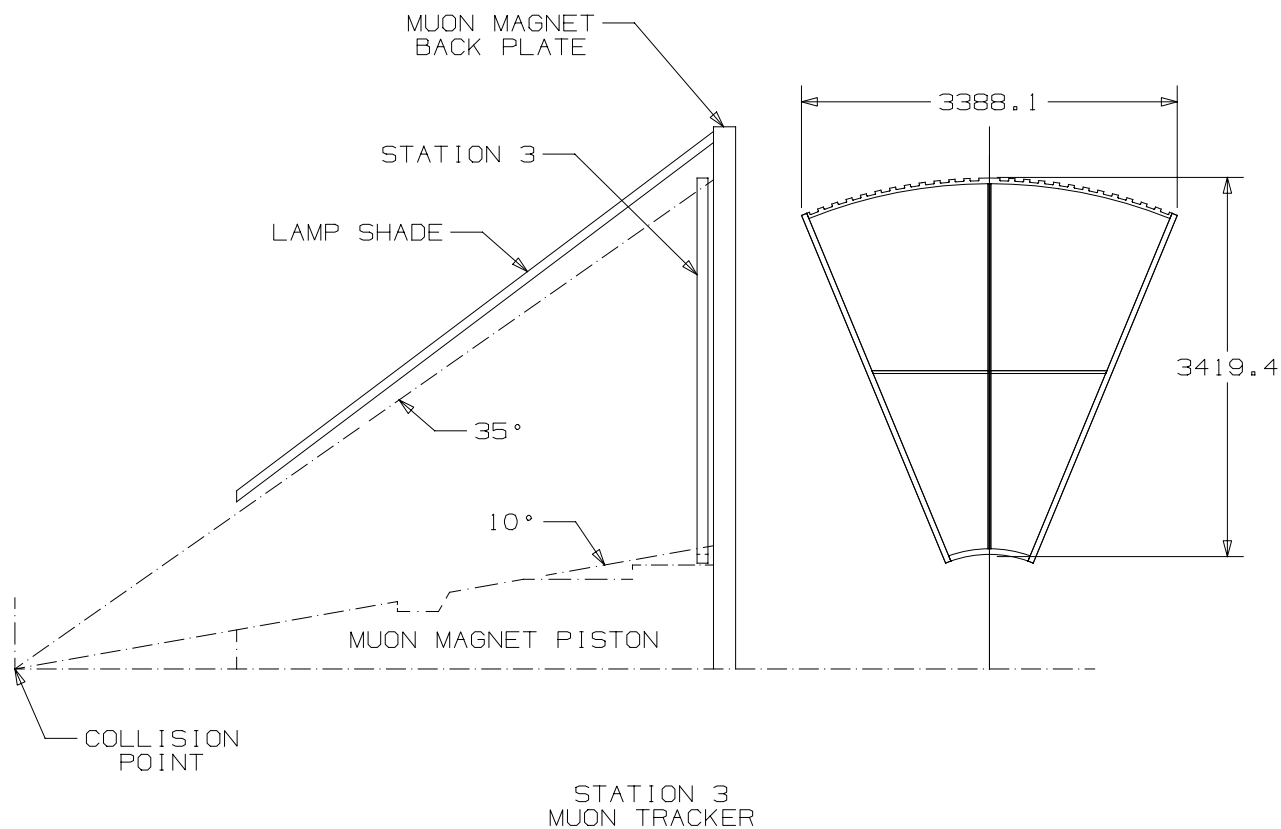
Figure 3.18: Preliminary Station 3 Design.

arrangement to form three CSC chambers. The thin frames are 7.5 cm wide and 3.43 mm thick consisting of a lamination of aluminum and epoxy fiberglass printed circuit board.

Similar to the station 1 design, the anode wires follow the chord in each 22.5° segment. The support spoke at 22.5° is attached to the top of the octant and free to slide at the bottom of the octant but is constrained to maintain the anode to cathode spacing to 50 μm. The spoke is constructed to form a laminate with one piece grooved to define the anode to field wire spacing and the cathode to anode spacing. A top cap is glued to the grooved piece to define the cathode to cathode spacing and to aid in making the spoke a more rigid structure. We anticipate using a material such as delrin. During the wiring process the anode spoke will be fixtured to maintain its correct position.

The CSC chambers are held rigid and in proper shape and position by two aluminum support structures 3 cm thick and 7.5 cm wide on either side of the thin CSC chamber frames. Nine alignment pins, three on each long edge, properly locate the thin frames during the assembly process. In addition, a single support structure is used during the etching and wiring process to insure proper location of the planes. A number of detailed calulations were performed to verify this design.
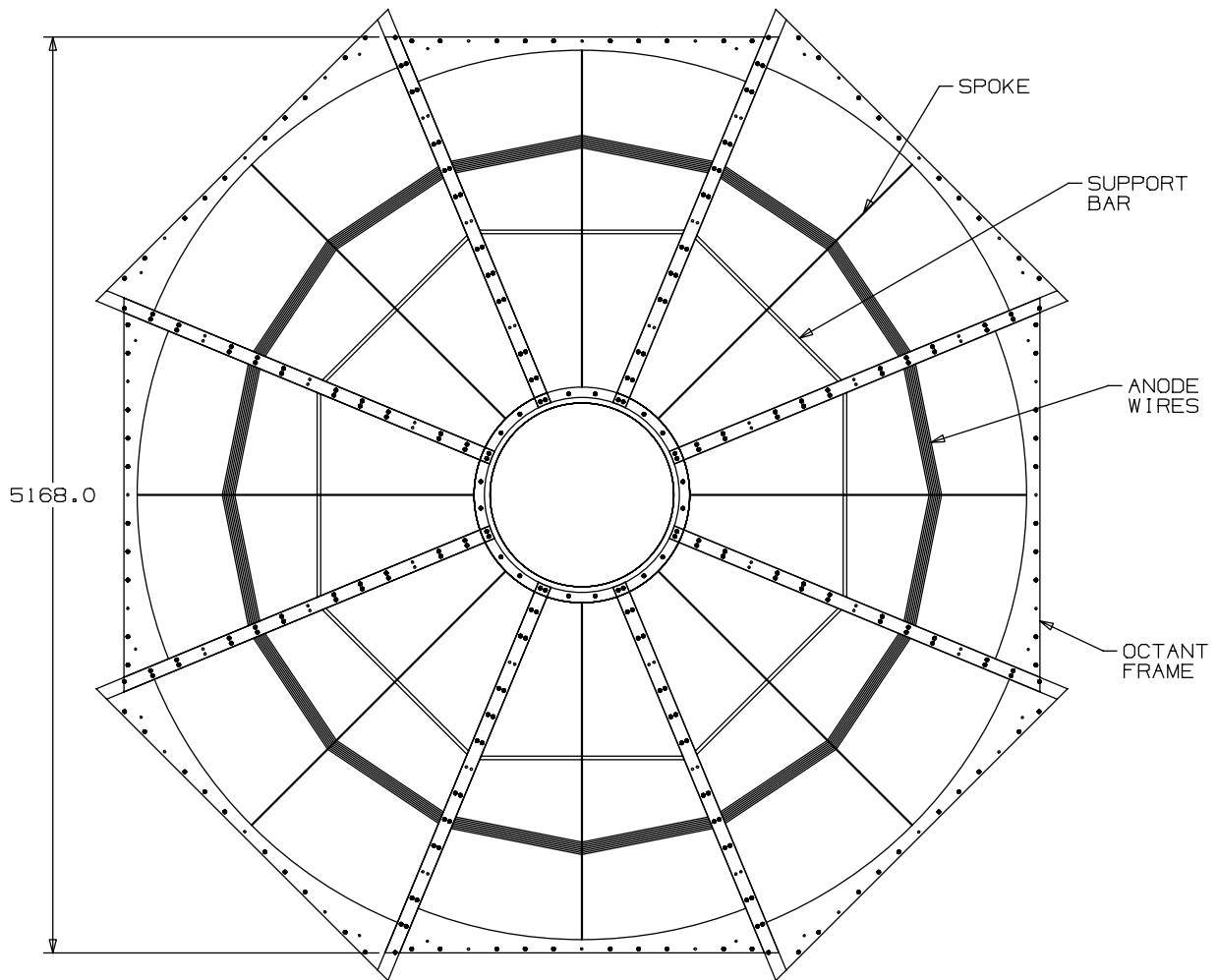
Figure 3.19: Station 2 View with All Quadrants.

Finite Element Calculations

Finite element calculations have been performed on the frame and frame support structure to understand distortions due to the wire and foil loads. The support frame is shown in Figure 3.20.

The support frame is fabricated from aluminum although aluminum was not our first choice for the support frame. Calculations showed that a carbon composite frame would provide substantial structural rigidity without the need for a cross member support but at an extremely high cost. The cost was projected to be $75k to $100k for each octant support thereby completely exhausting the entire station 2 budget. Therefore, efforts were undertaken to investigate stainless steel and aluminum as the support frame. The finite element analysis result for aluminum is shown in Figure 3.22. The maximum displacement
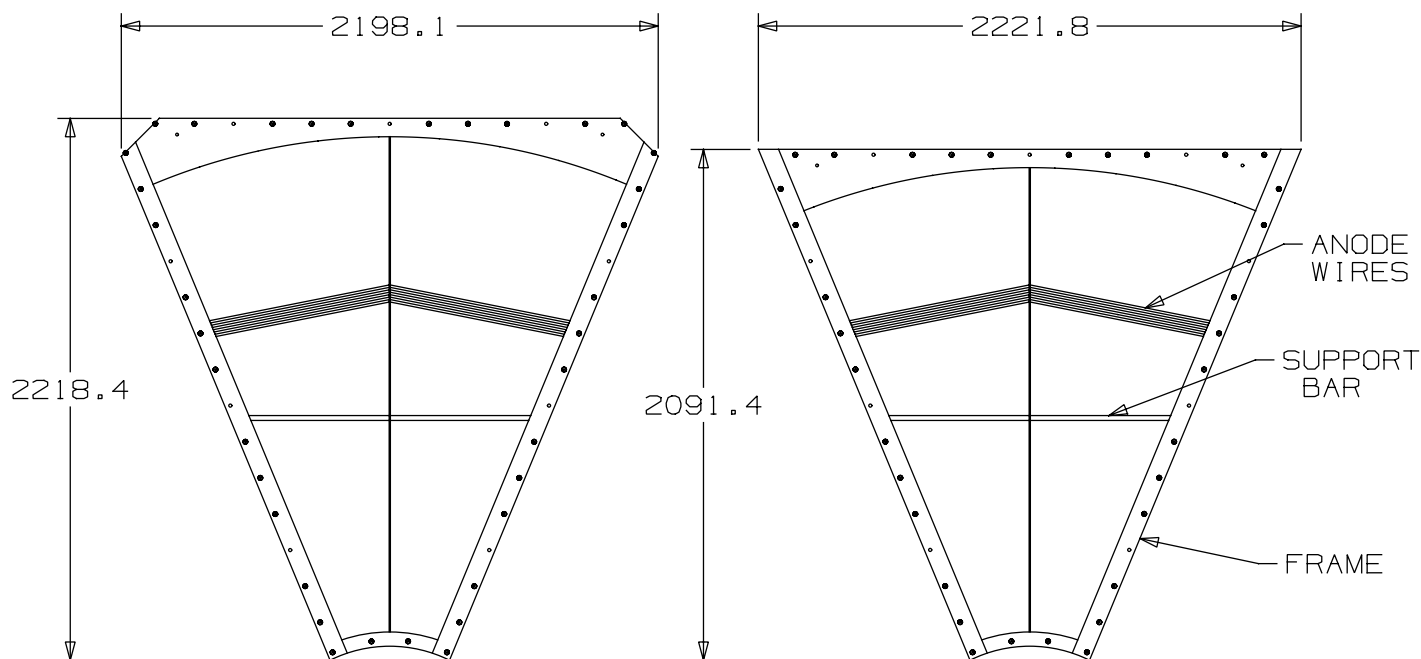
Figure 3.20: Station 2 Octant Design.

is 0.21 mm. Stainless steel of a comparable design had less displacement but at a price of three times the weight. We have established the baseline material to be aluminum.

Foil Etching

A technique to etch the thin kapton foil after the foil has been stretched on the support frame has been developed. This process involves electroetching the copper coated kapton with a probe tip attached to a low voltage source. The tip is mounted on a computer controlled $x - y$ table and positioned with an accuracy of 10 μm by a linear slide. A drawing of this setup is shown in Figure 3.23. The high resolution cathode will be prestressed during the etching process so that when the frame distortion occurs when all of the foils and wires are in place the cathode strips will be positioned correctly.

Since the kapton foil is available in widths up to only 1.5 m, station 2 must have foils that are glued together to get the required dimensions. A technique for gluing kapton foil was used successfully on cylindrical chambers for the MEGA experiment at LAMPF. They have not experienced any problems in three years. We have adapted this technique to the CSC foils and tests have been completed. Creep of kapton foils occurs in the first few days after stretching. Experience with full size stretched kapton foils have shown no unacceptable loss in foil tension due to creep over six months. Previously stretched 1 m foils have shown no loss in tension over four years. Generally, the foil will not sag under gravity load until the foil tension has almost fully relaxed. Our experience has shown this relaxation appears not to be a problem.
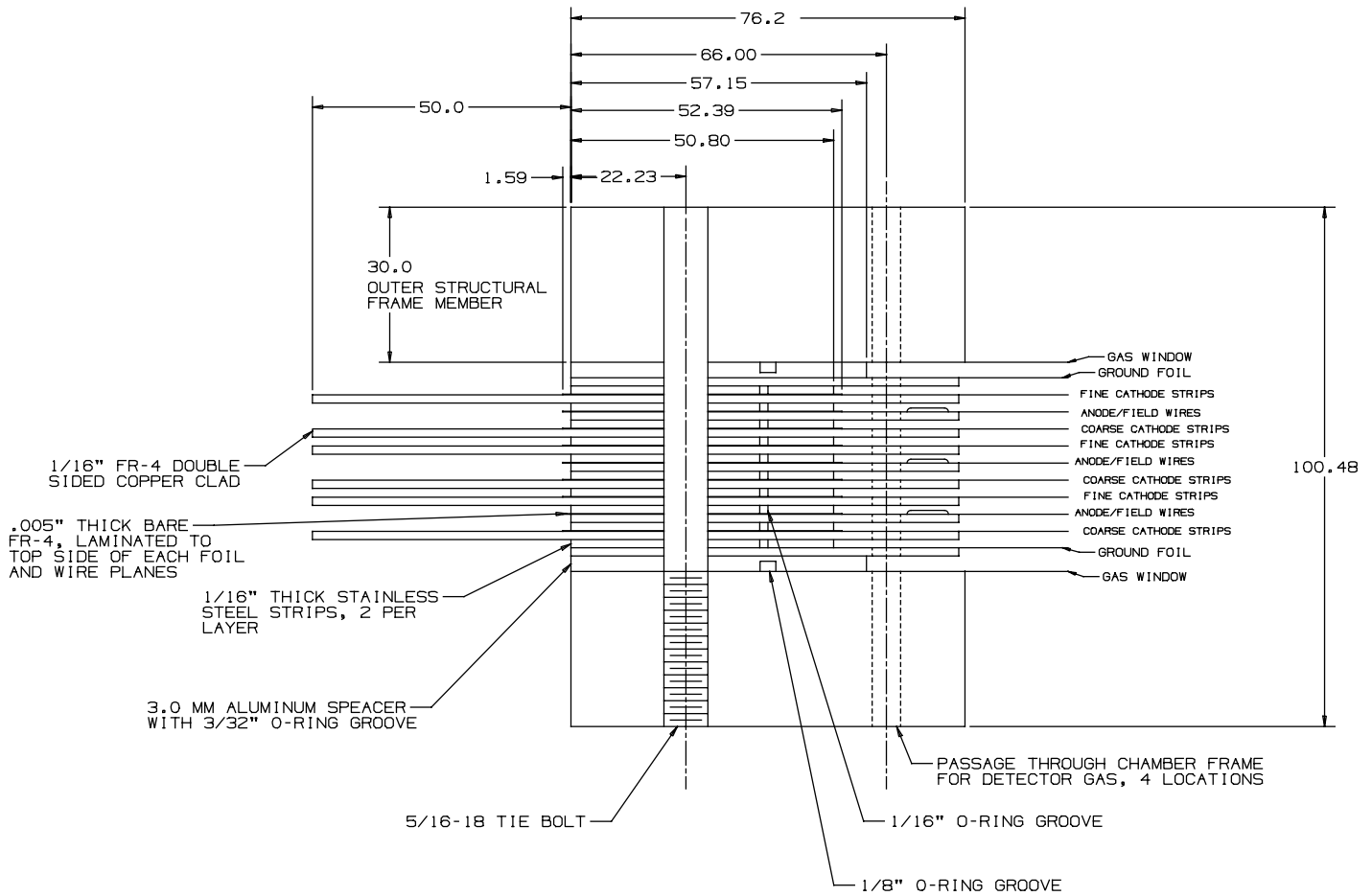
Figure 3.21: Station 2 Octant Cross Section View.

A foil etcher capable of etching the 2.5 m foils for station 2 has been assembled and tested. The positional accuracy of the optical encoders/lead screw has been measured to be <50 μm for the ϕ coordinate but only 200 μm for the radial coordinate. The reasons for the discrepancy are not known at this time but suspected to be in part due to uncertain manufacturing tolerances of the space frame and uncertainties in the straightness of the leadscrews. We expect these issues to be resolved in the future.

Station 2 Mounting structure

The mounting structure of the station 2 octants in the magnet must hold the octants rigidly over a short period of time (0.5 hours) when the active alignment system is incapable of defining relative positions of station 2 with respect to stations 1 and 3. The mounting structure is shown in Figure 3.24 as viewed from the front and in Figure 3.25 as viewed from the side. It consists of stainless steel tubing, rectangular in shape, on the front and back of

Lin DISP Lc=1

MECHANICAL PARAMETERS
AND CALCULATION RESULT   PHENIX PROJECT

MATERIAL: AL_6061   PROTOTYPE MUON CHAMBER FRAME
RADIAL PRESSURE:
        27.06 LBS/IN
TANGENTIAL PRESSURE:

        21.80 LBS/IN

STRUCTURE:
TOP BEAM WITH FLAT TOP
AND ARC SHAPE (R=2509MM)
BOTTOM BEAM: 50MMX30MM
SIDE BEAM: 75MMX30MM
SUPPORT BAR: 20MMX30MM

MAX. DEFL: 0.2148MM
AT MIDSPAN OF TOP FRAME

MAX. DEFL: 0.081MM
AT MIDSPAN OF BOTTOM FRAME

ABSOLUTE DISPLACEMENT AT
BOTH ENDS OF SUPPORT BAR IS
UX=0.0675MM
UY=0.0277MM

FILE NAME: PHENIX_A
DATE: NOV. 6 1994
LANL/ESA-DE Z.CHEN

Figure 3.22: Results of finite element analysis of CSC frame.

the octants with a truss structure at the top and mounting ring at the inner radius. The mounting ring does not come in contact with the piston. It is mounted to the magnet at four points at the bottom of the magnet and at four points to the teacup. The mounting structure, and therefore the chamber octants, are electrically isolated from the magnet.

The mounting structure design criteria was to have vibrations from natural frequencies less than 25 μm. Static distortions due to gravity, thermal, and magnetic effects were minimized but allowed. The active alignment system is designed to account for static distortions.

An analytic calculation of the weight and maximum distortions of the space frame were carried out for a variety of tubing sizes and for stainless steel and aluminum. The results pointed to stainless steel with a cross section of 7.5 cm $\times$ 5.0 cm $\times$ 0.3175 wall as an acceptable material. The maximum displacement under gravity load is 0.399 mm. We were constrained to have the frame and chambers fit in the piston slot of 35 cm. This design is 30 cm. A finite element analysis of the mounting structure with the octants in place has
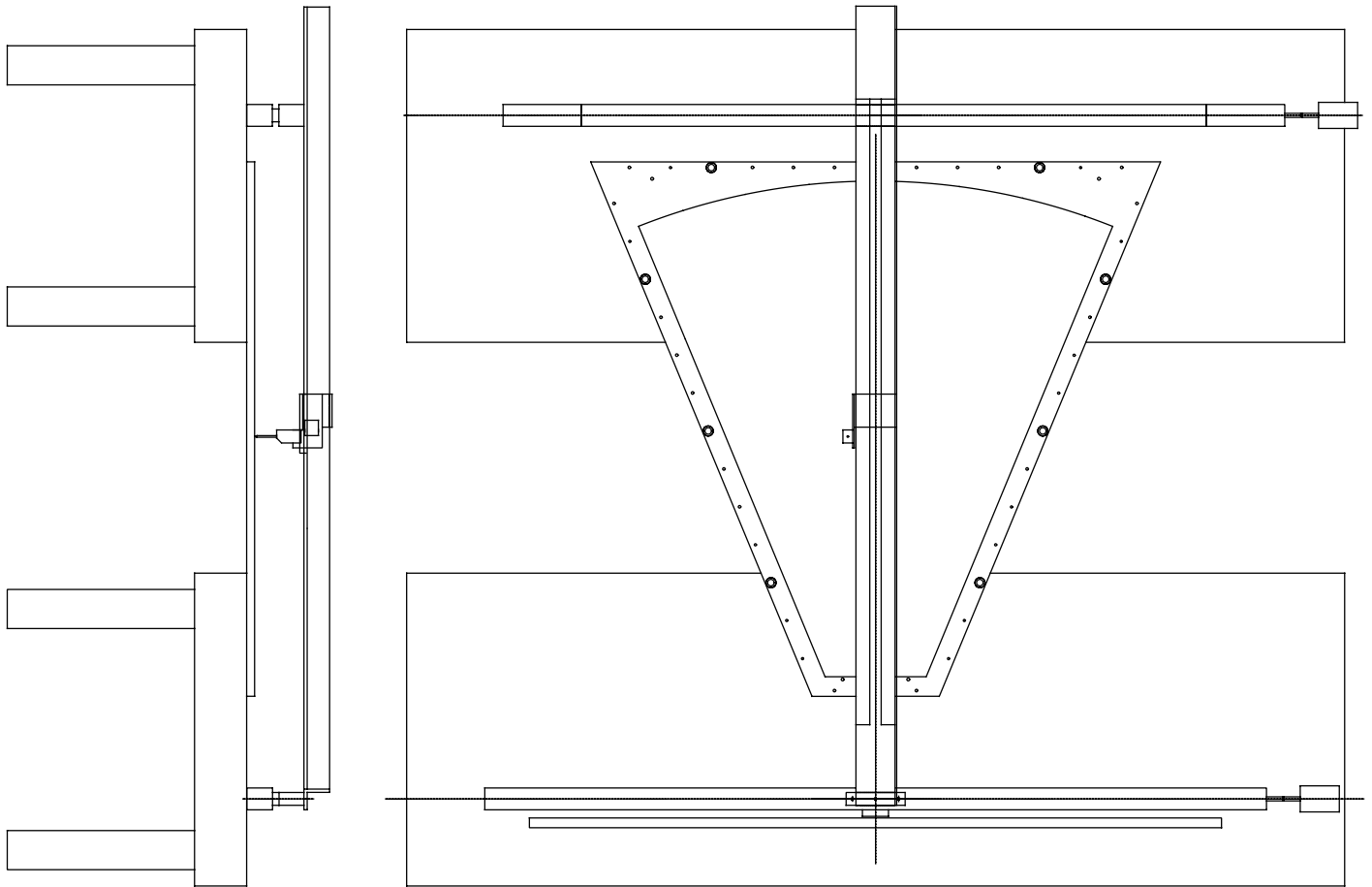
Figure 3.23: Setup for etching stretched cathode foils on frames.

Mode #	1	2	3	4	5
Freq (Hz)	7.9	12.4	16.6	25.5	27.9

Table 3.4: Frequency Results.

been carried out with the program COSMOS/M to define the natural frequencies of vibration and the static distortions due to gravity. The static distortions due to gravity are shown in Figure 3.26. The maximum distortions were 0.362 mm. The frequency results are shown in Table 3.4.

The first three modes correspond to displacements in the z direction. The fourth and fifth modes are displacements in the ϕ and r direction and therefore are of greatest concern. To determine the maximum displacements expected from these and all frequecy modes, a dynamic analysis was done using the finite element analysis program ABAQUS. The excitation to the station 2 structure was based on measurements made at four laboratory facilities

16 ALIGNMENT
HOLES

6066.1

FRONT VIEW

STATION 2
MUON TRACKER
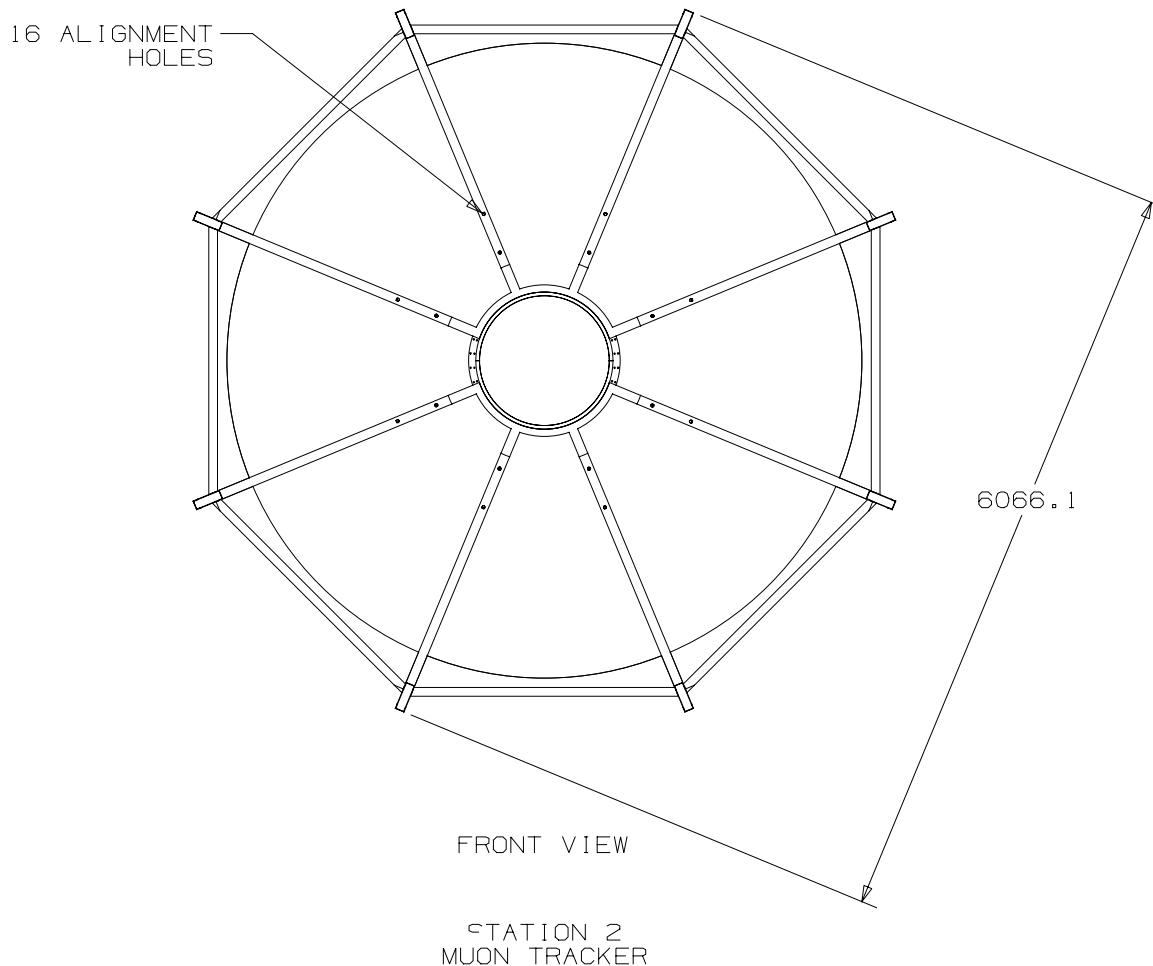
Figure 3.24: Station 2 Mounting Structure - Front view.

[33]. It was considered roughly typical of what one would expect at the PHENIX facility. No site specific ground motion measurements have been made and the excitation function does not represent vibrational forces that could be generated by equipment (e.g. vacuum pumps, etc.) attached directly to the PHENIX detector. In the calculation the sagitta error was determined under the assumption that stations 1 and 3 are fixed. The frequency analysis for the magnet suggests that motion in the x and y coordinates of stations 1 and 3 is negligable owing to the large massive backplate and teacup to which they are attached. The response power spectral density for x and y components of the sagitta at one particular node (node 40) is shown in Figure 3.27. This node corresponds to the vertical frame of the octant at the top of the magnet at the 12:00 o'clock location. The peaks in the spectrum correspond to the frequecies where the coupling is the largest. The z component is added for reference but does not effect the sagitta. The largest x component of the sagitta rms response is 0.17 μm at node 40. The largest y component of the rms response is 0.11 μm at node 6. Node 6 corresponds to the horizontal frame of the octant on the side of the magnet at the 3:00 o'clock location. The largest z component of the rms motion relative to the base

360.0

RIGHT SIDE
VIEW

STATION 2
MUON TRACKER
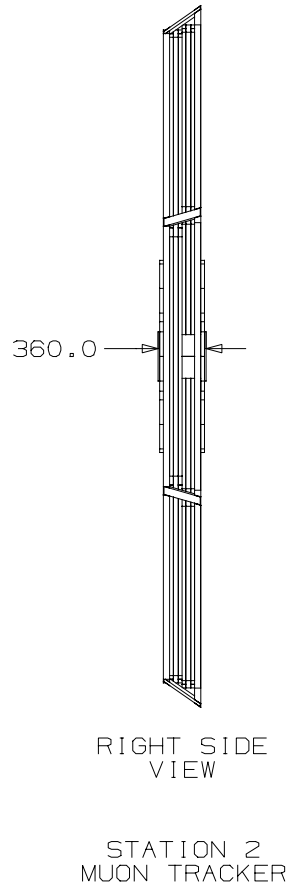
Figure 3.25: Station 2 Mounting Structure - Side View.

is 1.1 μm at node 260. Node 260 corresponds to the horizontal member at the top of the octant at the top of the magnet. The modes that cause the greatest x direction motion are modes 4 and 5. The mode giving the greatest z direction motion is mode 1. The modes that give the greatest y direction motion are modes 1, 4 , and 5. Mode 1 involves primarily z direction motion, but some coupling occurs to y. The results show that the largest sagittal error introduced because of ground motion is approximately 0.2 μm. We expect to measure the ground motion at the PHENIX site and redo this calculation but the results indicate that we have two orders of magnitude margin before ground motion becomes a problem.

3.3.7   Global Tracking System Design Issues

To satisfy the physics requirements of the tracking system, the assembly plan for the detectors, the alignment requirements, and the calibration requirements have to be addressed.

Assembly Plan for the Detectors

The CSC detectors will be assembled precisely primarily by using highly accurate positioning jigs. For stations 1 and 3, the alignment of the high resolution cathode will be accomplished

```
Lin DISP Lc=1
SPACE FRAME AT STATION 2
WITH MUON CHAMBER STIFFNESS ON
LOADING: GRAVITY
MATERIAL: ST_ST
MAX. DISP: 0.363 MM
```

Disp_Res

-0.000363

-0.000318

-0.000273

-0.000227

-0.000182

-0.000136

-9.09E-05

-4.54E-05

-1.00E-16
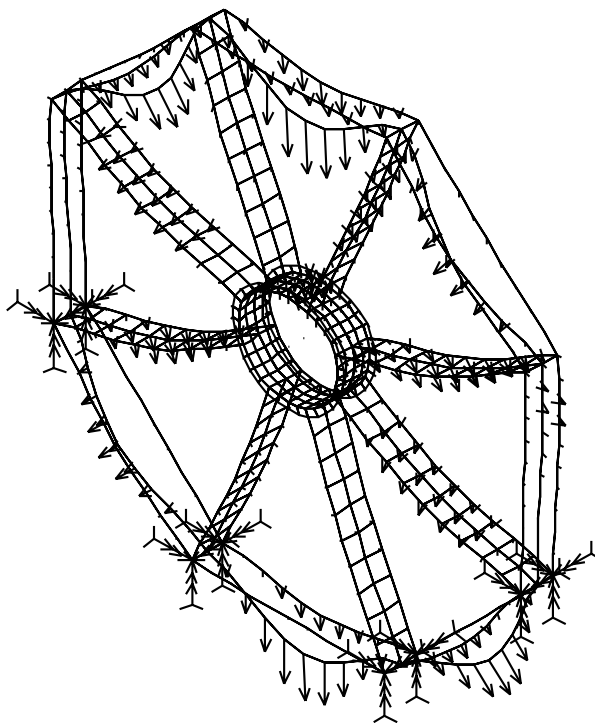
Figure 3.26: Static Distortions of station 2 Due to Gravity.

by using a drilling jig to locate the hole for the alignment pins to the cathode strips. For station 2, the precision of the strips to the alignment pins will be dominated by the accuracy of the etching table, 25 μm. In addition, for station 2 we will etch a ground foil with alignment fiducials that are visible external to the chamber. The location of these fiducials will be determined during the staging of station 2 in the chamber fabrication building prior to installation in the magnet and again when installed in the magnet. The active alignment system will provide the accurate survey in the magnet and will determine subsequent motion due to thermal effects and field effects.

Alignment Plan for the Detectors

It is our goal for the tracking chambers to define the contribution to the station resolution to be as small as possible consistent with expected alignment and assembly errors. A detailed report on the contributions the errors and alignment and assembly is given Ref. [34]. In summary, we expect the assembly errors to be 25 μm, the alignment errors to be 10 μm, and the calibration of the alignment system to be 25 μm. The combined errors with 100 μm intrinsic chamber resolution gives a realizable chamber resolution of 110 μm. To achieve a
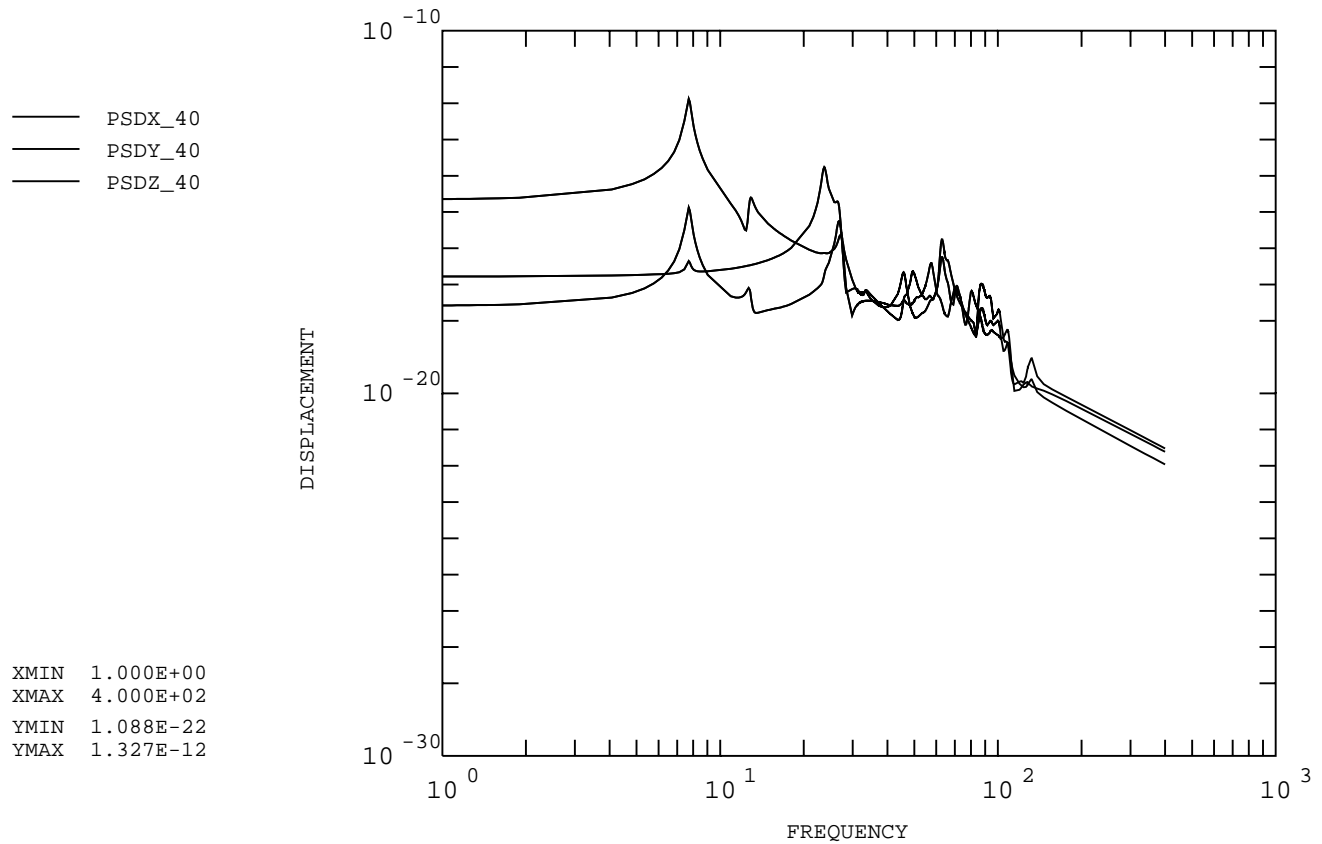
Figure 3.27: Power Spectral Density Sagitta Response for x and y directions at node 40.

realizable chamber resolution of 100 μm, an intrinsic resolution of 82 μm is required. Either resolution is acceptable. Every technique to improve the chamber resolution and the other combined errors will be implemented. The single largest contributor to the resolution is the chamber resolution and this is primarily due to electronic noise and calibration. Our greatest effort will be directed at reducing the electronic noise and insuring that the calibration scheme between channels is very accurate.

3.3.8   CSC R&D Prototypes and Results

The major issues for the CSC chambers involve the mechanical construction of the chambers, the electrostatic stabliity, and resolution.

Chamber prototypes

The prototype PHENIX chambers are all full scale prototypes to streamline the R&D. The station 2 prototype consists of a single CSC plane. The structural frame is the same as shown

in Figure 3.20 and the cathode foils and anode planes are the same as shown in Figure 3.21. The support frames were built and found to be within the 25 μm tolerance for the alignment pins. Full scale foil frames were constructed and stretched with gold and aluminum coated kapton foils. The technique of using laminated aluminum and epoxy fiberglass frames with glued joints have been successfully tested. The seamed 25 μm copper coated kapton foils were stretched and etched without problems. We have successfully transferred the alignment pin holes to the thin foil frames by using drill guides in the support frame and the support frame as the template. We have yet to test the anode support spoke. The maximum unsupported anode wire length in station 2 is approximately 1.15 m.

Station 1 prototype chamber is full scale with two CSC chamber gaps. Two hexcel panels were constructed by a commercial vendor and one hexcel panel was constructed "in house". The commercial vendor found no problems with the 150 μm flatness tolerance but the estimated cost of the commercial panels is twice that of the "in house" panels.

A full-scale Station 3 prototype chamber was constructed. It consisted of one plane of cathode readout.

Resolutions

The resolution of 100 μm has been achieved in both the Station 2 and 3 prototypes. We, therefore, turn out attention to issues of calibration which will establish how well we will achieve the desired resolution in a full system of chambers.

We believe that our assembly procedures are adequate. The electronic noise level is a concern since the strip capacitance is very large. However, a recent amplifier design [35] has been fabricated that meets or exceeds all of our requirements. The measured noise level at the maximum capacitance of our chamber strips exceeds our noise level requirement by 2.5 and meets our linearity requirements. The remaining concerns are calibration and assembly. The calibration can be accomplished by injection of a precise charge into the amplifier by either a capacitor incorporated into the front end amplifier or an external capacitor etched into the PC board. Etching a capacitor into the PC board depends on the accuracy of the etching process but we expect to be able to do this to the 0.5% level. We need 1% accuracy so this technique should work.

Mechanical R&D

The major concerns for the mechanical design are achieving 150 μm flatness of the honeycomb panels, achieving good electrostatic stability and therefore good efficiency plateau for our choice of mechanical design and unsupported anode wire length, verifying the anode support spoke for the station 2 design, and generally testing that the assembly procedures are adequate to maintaining the resolution requirements.

3.4   Muon Identifier Detectors

3.4.1   Detector Design Optimization

Steel Thickness

The irreducible μ/π ratio due to weak decay is approximately 1×10^{-3} (primarily determined by the proximity of the nosecone to the vertex). We set a detector design criteria to 1/4 of this, namely 2.5×10^{-4}, for a pion from the vertex to be misidentified as a muon (forming part of a dimuon). The factor of 1/4 provides over an order of magnitude suppression for the *pair* background. Thus, the irreducible background of muons reaching the muon identifier, as opposed to the muon identifier design and the algorithms used to reject the larger hadron background, will set the ultimate physics background level. Of this required net μ/π separation, approximately 10^{-2} is provided by the presence of the absorber preceding the muon identifier which filters out pions. This leaves 3% as the maximum tolerable fraction of the charged pions which may subsequently be misidentified as muons.

The punchthrough probability versus depth of steel for muons of various momenta are plotted in [36] and [37]. In order to set the punchthrough probability for muons of up to 4 GeV/c to be 3% or less, a total steel depth of 90 cm (5.4 hadronic interaction lengths) is required beyond the nosecone and central magnet. Subtracting the thickness of the muon magnet backplate, a total depth of 60 cm of steel is required in the muon identifier itself.

A muon at the vertex must have a mean energy of at least 1.9 GeV to reach the muon identifier system. The mean minimum original energy to penetrate completely through the muon identifier is 2.7 GeV [38].

Number of Layers

Ideally, the 60 cm of steel is to be distributed in a sandwich interleaved with detector layers. The detectors themselves require a non-negligible amount of space and the total available space in z is quite limited in the PHENIX detector hall (2.7 m). Also, it is desirable to have the early absorber layers be divided more finely to increase the acceptance for ϕ meson detection. Segmentation also improves the measurement of the trajectory in the identifier. The segmentation chosen is a total of four steel absorbers after the 30 cm thick muon magnet backplate of the north arm of thicknesses 10, 10, 20, 20 cm. The 5 gaps created by the absorbers are instrumented with the muon identifier panels. The muon identifier for the south arm is identical to that for the north arm (although the muon magnet backplate is only 20 cm thick) and at the same distance from the interaction vertex. Maintaining the same design for both arms helped minimize design costs.

Readout Pitch Requirements

Beam gas studies show that for low polar angles (20° or less), an effective segmentation into logical pads of approximately 13 by 13 cm is required to suppress false roads for tracks in the muon identifier. Rather than develop Iarocci tubes of greater width or use 13 cm wide external strips, the most cost effective solution is simply to use standard Iarocci tubes of

width 8.5 cm with all eight internal wires ganged together. This provides a readout pitch of 8.5 cm along both the x and y directions, thus providing effective 8.5 cm square hodoscopic cells (upon forming the appropriate ANDs). This most cost effective solution exceeds our requirements. This segmentation is fine enough to provide sufficient granularity for matching roads in the identifier to tracks in the muon tracker unambiguously with anticipated occupancies.

3.4.2 Introduction to Iarocci Tubes

What They Are

We use the term Iarocci tubes to refer to planar drift tubes consisting of 100-μm gold-coated CuBe anode wires at the center of long channels of a graphite-coated plastic cathode, with a gas mixture such as Isobutane-CO_2. This same physical detector when operated at higher voltage is a conventional limited streamer tube [39]. We operate them in the proportional mode to increase longevity. They are proportional tubes operated at a voltage such that only a fraction of the signals are not proportional mode pulses.

How They Perform

We apply 4500 V to the anode wires. Incident minimum ionizing particles ionize the gas and create an avalanche. Using a high voltage decoupling capacitor, we read out the signal on the anode wire. The drift time interval (for arrival of 90% of pulses) in the tube is approximately 100 ns for a 9:91 Isobutane-CO_2 gas mixture.

Why They Were Chosen

Iarocci tubes were chosen because they satisfy all of the detector performance criteria discussed above. They have proven reliability and longevity, compactness, low cost, and are readily available from commercial vendors [40]. Such tubes can be used economically to tile large areas. They have robust wires and seals. They avoid the problems of metal-plastic transitions present at the endcaps for aluminum proportional tubes.

Tubes with 9 mm by 9 mm channels satisfy the count-rate and position localization requirements, but must be staggered by half a cell and ORed in pairs (discussed below) and/or operated with a fast gas (discussed below) to meet the timing requirements of the Local Level 1 (LVL-1) trigger system.

3.4.3 Design of Muon Identifier Detectors

Definition of Terms

A Channel: An individual anode wire and the immediately surrounding gas volume and graphite-coated walls are referred to as one channel of an Iarocci tube. Each wire is held at

| A | B | C |
| D | E | F |

Table 3.5: Panel arrangement viewed from origin.

Panels	Horizontal	Length	Vertical	Length
A,C,D,F	118H	5200 mm	128V	5010 mm
B,E	90H	2504 mm	52V	3821 mm

Table 3.6: Number and lengths of Iarocci tubes per panel.

the center of its channel by means of plastic wire spacers positioned every 50 cm along the tube.

A Comb Profile: The three sides of each of the eight channels in an Iarocci tube are provided by the graphite-coated comb profile.

A Jacket: The (outer) jacket is the surrounding rectangular PVC housing that encloses the comb profile to create the gas-tight box for the eight channels.

A Tube: The term Iarocci tube refers to the ready-to-go detector element consisting of eight channels. Its principal components are the comb profile, the wire, wire spacers, outer jacket, and plastic endcaps.

A Two-Pack: A two-pack is a pair of tubes connected together and staggered by half a channel. Their signals are OR'd together.

A Panel: Groups of two-packs oriented both horizontally and vertically are held inside an aluminum box. Approximately half are oriented horizontally and half are oriented vertically so that both projections are measured. This total detector element is called a muon identifier panel. There are six such panels per gap labelled A through F as shown in Table 3.5.

Layout of Panels In the Detector

The number and lengths of tubes inside every panel are listed in Table 3.6. Overall specifications are listed in Table 3.7. Adjacent panels overlap along their edges to eliminate the
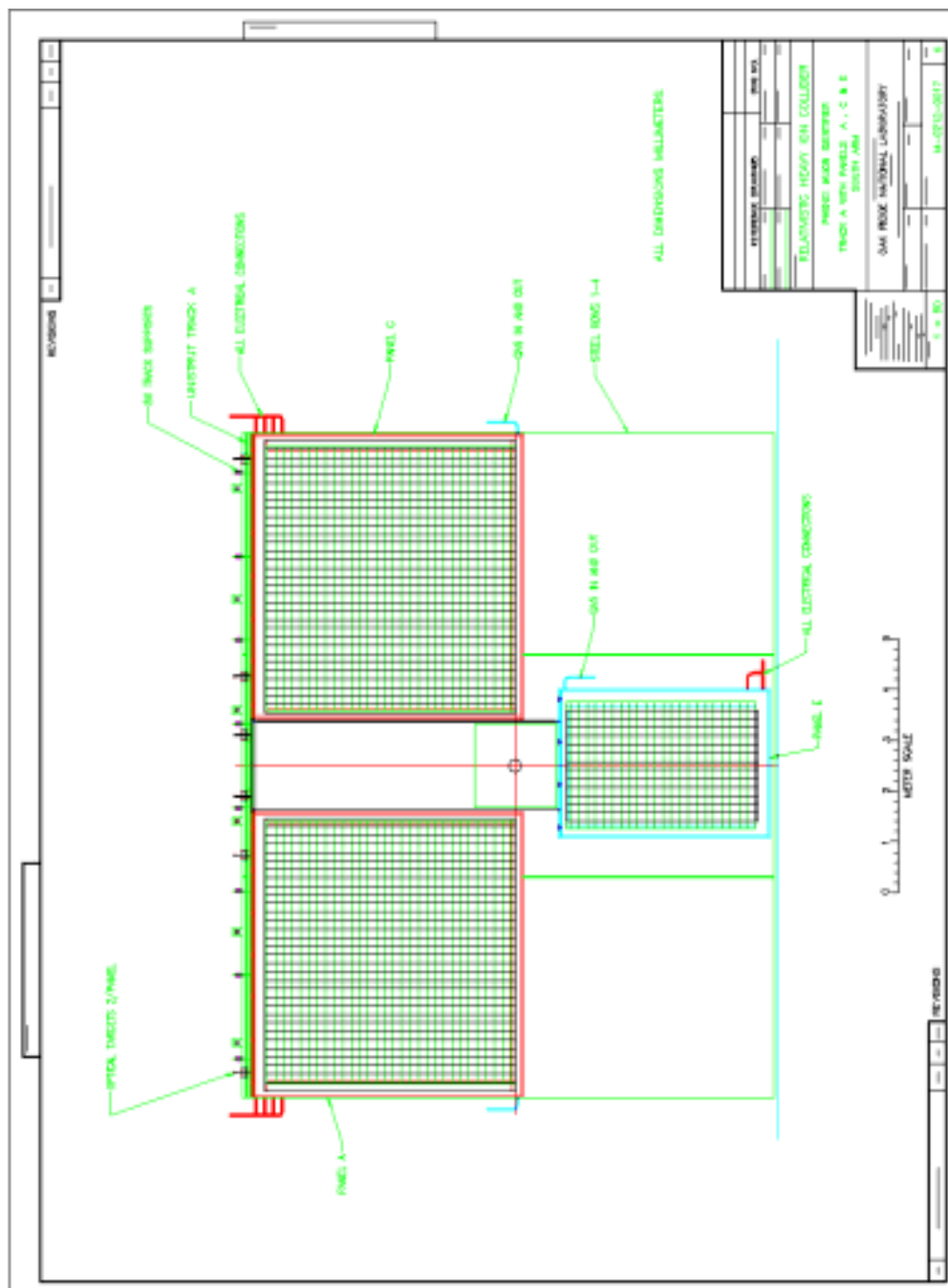
Figure 3.28: Muon identifier panel arrangement.
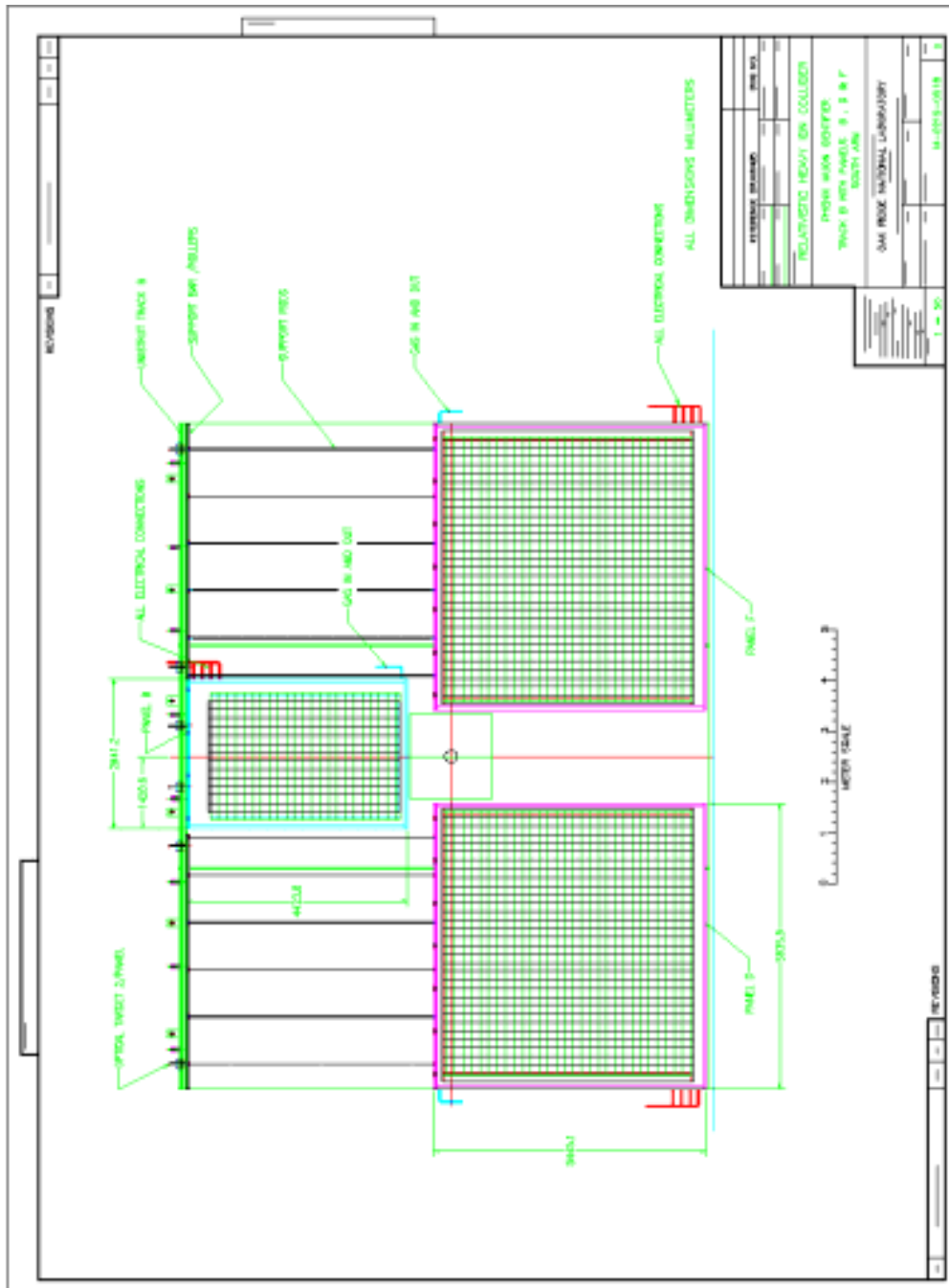
Figure 3.29: Muon identifier panel arrangement.
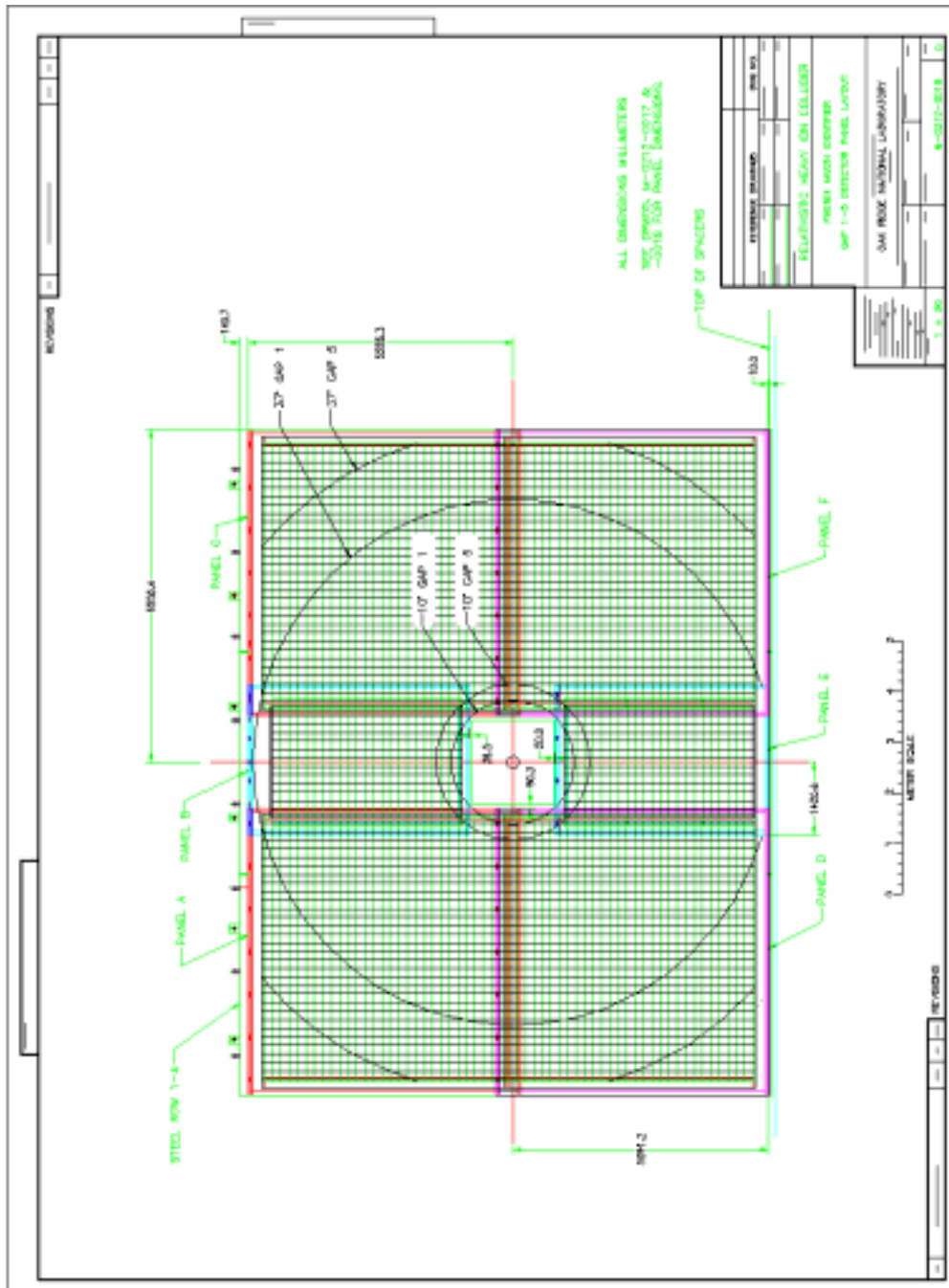
Figure 3.30: Muon identifier panel arrangement.

Quantity	Value
panels/gap	6
panels/arm	30
tubes/gap	1268
tubes/arm	6340
area/gap	13.1 m × 10.7 m

Table 3.7: Muon identifier specifications.

creation of any deadspace by the panel frames. The panel frames are shown in Figure 3.28. Panels (A, C, and E) lie in one plane which is 10 cm closer to the vertex than the plane of the other panels (B, D, and F).

The muon identifier has panels hanging in two parallel rails attached to the MuID steel in a given gap. Figure 3.28 shows panels A,C and E, all of which hang in a single rail. The lower panel E hangs from two rods which are secured to the rail just to the inside of panels A and C. The connection points for gas and electrical services are shown, as are the optical survey targets.

Panels B, D and F all hang in a single rail as shown in Figure 3.29. The lower panels each hang from six rods which are secured to the rail. The connection points for gas and electrical services are shown, as are the optical survey targets.

Figure 3.30 shows the active area of the (two-packs) of Iarocci tubes oriented vertically and horizontally in the eight detector panels of one gap. The 7 cm thick aluminum panel frames and the top support rail are shown. The figure shows where 10° and 37° cones would reach for both detector gaps 1 and 5. As is apparent, the acceptance reaches down to 10° in the first plane (and even farther in subsequent planes) except immediately at the four corners of the square beam hole. The elevation view of the north muon arm is shown in Figure 3.31.

3.4.4   Muon Identifier Design System Issues

Assembly Plan for Muon Identifier

The tubes are assembled off-site by a commercial vendor and shipped to our assembly factories located BNL and KEK after having satisfactorily passed quality assurance tests for both gas leakage and high voltage. The tubes are installed into panels at our factories. The assembled and tested muon identifier panels manufactured at BNL will be transported by truck a short distance to the Main Facility Hall. Those assembled in Japan are shipped by cargo ship to BNL. Each will be attached to a special exterior handling frame that can be hoisted using the hall crane. The panels will be inserted in appropriate sequence onto the rails of each gap in order to achieve the desired arrangement. The shield wall ultimately prevent removal of panels.
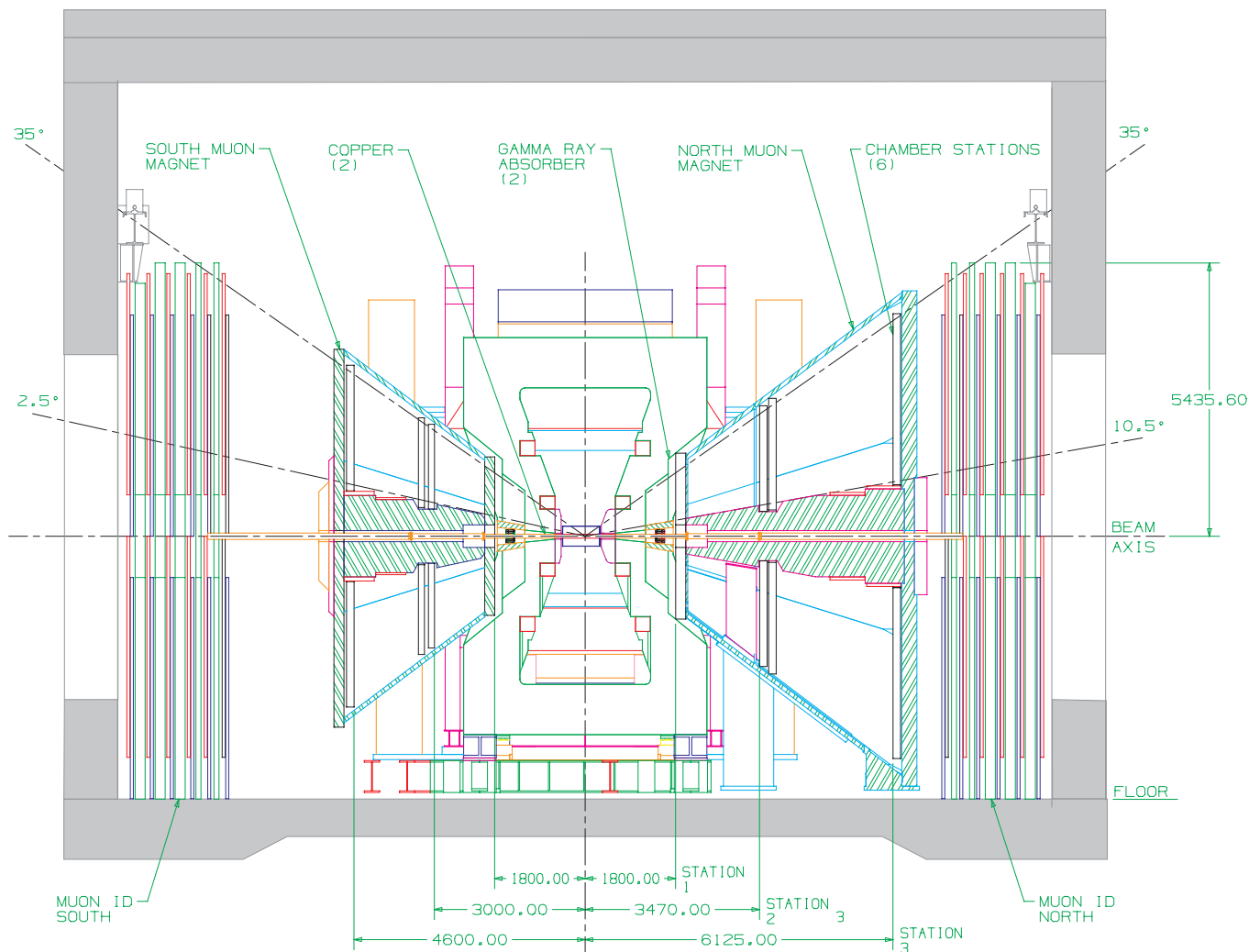
Figure 3.31: Elevation view of Muon Arms.

Timing Requirements for Triggering

We require a drift time interval shorter than the time between beam collisions (106 ns) in order to avoid dead time. Shorter drift times reduce the backgrounds associated with the arrival of out-of-time hits such as upstream beam gas events as well as relaxing constraints on the electronics that feeds the LVL-1 trigger system (by providing margin for variations among tubes, cable delay variation, open/closing of latch, drift from cell edge, and time-of-flight from vertex).

Alignment Requirements

The muon identification system has much less stringent alignment to the vertex requirements than the muon tracker since the typical pointing resolution of the system is measured in centimeters and the muon identifier's main function is to work with the muon tracking system. However, since the muon identification system is used in the trigger to find roads which point back to the vertex, there must be some relative alignment of the identifier panels with the interaction point.

The multiple scattering in the absorber material in front of the muon tracking stations limits the angular resolution of a 10 GeV/c track at the vertex to approximately 3 mrad or more. If this error is projected from the first tracking station to the muon identifier, the position resolution is approximately $(5.4 \text{ m}) \times (3 \times 10^{-3}) = 1.6$ cm. An additional 1 to 2 mm or error occurs at each of the absorber layers in the muon identifier. Therefore, the muon identifier planes need not be surveyed with respect to the vertex to better than approximately ± 4 mm in the x and y directions in order to have alignment errors be negligible compared to multiple scattering errors. It is only required that the z positions be measured after they are installed, and this measurement only has to be known to within a few centimeters relative to the vertex.

To Tracking System   The effective logical pad sizes represented by the transverse tubes of the muon identifier system are 8.5 cm by 8.5 cm. The position resolution along a muon identifier road cannot be expected to be much better than $8.5/\sqrt{12} = 2.5$ cm. If several measurements of resolution 2.5 cm are used, then a projection error of somewhat less than 2.5 cm might be expected. Multiple scattering due to the 30 cm thick muon magnet backplate causes a projection error of 2 mm for a 10 GeV/c track in the tracker to the beginning of a road in the first plane of the muon identifier. We require alignment of the muon identifier planes with station 3 of the tracking system to ± 1 cm in the x and y directions.

Internal   The internal alignment requirements of the muon identification system are determined by its ability to form roads when the tubes are misaligned by a given amount. The individual tubes are 8.5 cm wide. We require alignment errors to be a negligible contribution to the projection error of a road from one plane to the subsequent planes in the identifier system. We require a 5 mm panel to panel alignment in order for road finding in the muon identifier to be limited by multiple scattering. Within a four-pack, we require and can easily achieve a stagger by half a channel to within 1 mm.

Method of Alignment

The tubes are installed and surveyed within each panel relative to external fiducial marks on each panel to within an accuracy of 2 mm. The external fiducials of the panels can be viewed by conventional survey theodolites located along the west or east sides of the respective arm and down the the main square hole which contains the beam pipe. Using standard survey techniques it is straightforward to measure the absolute positions of the muon identifier detectors to within 3 mm or less which often exceeds our requirements. Panel positions

can be adjusted by sliding transversely and by means of lowering rods; however, in most instances we just need to *know* the as-built as-installed positions. Further details concerning muon identifier alignment criteria are discussed in [34].

Calibrations for Muon Identifier

We will record calibration data to obtain samples of cosmic muons, samples of beam gas muons, pedestals, to set discriminator thresholds, monitor timing alignment, monitor HV stabilization, and monitor efficiencies.

3.4.5   R&D Results

We have studied the characteristics of resistive plate counters (RPC) and Iarocci tubes operating in both the proportional and limited streamer modes in order to make a technology choice for the PHENIX muon identifier sytem. The conclusion of this study is that Iarocci tubes are best suited for this application. The R&D results and technology choice are described in Ref. [40].

Pulse Height Studies

We have measured the pulse heights for signals (from cosmics and radioactive sources) using different gas mixtures, different channel widths, and different operating voltages [40]. We have studied the plateau width versus high voltage, pressure dependence of pulse height, proportional mode running, and limited streamer mode running.

Timing Studies

The drift time interval for conventional 9 mm by 9 mm LSTs with a standard gas (Ar-isobutane) is approximately 100 ns which is too long for our application because it is of the same order as the RHIC bunch crossing time (106 ns). (The rise time and pulse duration are satisfactory, however.) We studied and achieved faster timing characteristics by ORing pairs of tubes in a two-pack staggered by half a channel. We thus are able to construct a viable muon identifier using a conventional gas. Note that an important additional reason for the stagger is that it reduces the geometrical inefficiency due to the comb profile septa from 10% to near zero (at normal incidence).

We investigated two other means of obtaining shorter drift times by using faster gas mixtures including CF_4 and by developing Iarocci tubes with a 5 mm by 5 mm cross section, instead of the standard 9 mm by 9 mm as discussed in [40].

We are interested in the efficiency of the two-packs within a timing window of 81 ns (where 81 ns represents the 106 ns between collisions reduced by 25 ns for flip-flop settling and 10 ns for signal transit variation along the length of a tube). Figure 3.32 shows that at 81 ns, the two-packs are measured to have only a 5% inefficiency when operated with a 9:91 mixture of Isobutane and CO_2.
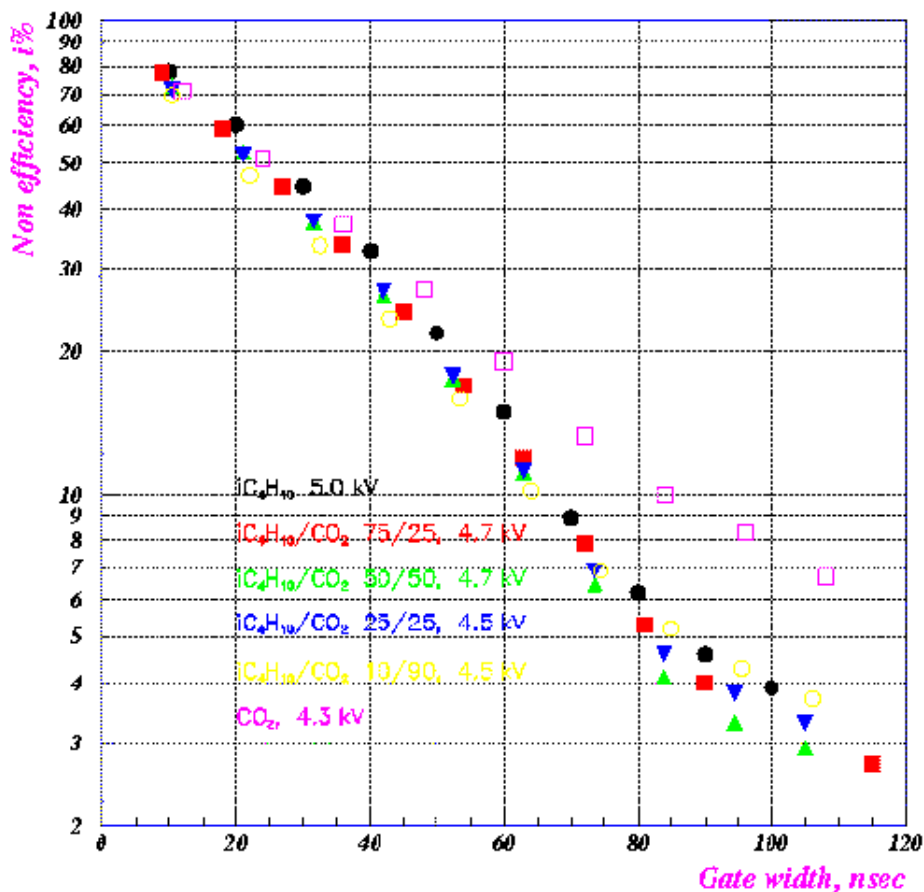
Figure 3.32: Gas timing studies.

Beam Test Results

A series of beam tests (RD93, RD94) were performed at the AGS to study the performance of Iarocci tubes [40]. A prototype muon identifier was prepared for the June 1993 AGS test beam run on the B2 line. The purpose of this prototype was to build a section of muon identifier that was more finely segmented in both longitudinal and transverse directions than planned for PHENIX. Analysis of test beam results were compared with GEANT simulations as well as simulations of performance of the planned PHENIX muon identifier configuration.

The prototype muon identifier was composed of steel plates stacked to form a sandwich of ten layers with gaps between each layer for the detection system to be inserted. The detector was choosen to be Iarocci type gas tubes operated in the limited streamer mode. The signals were read out by x-strips on one side of the tube array and by y-strips on the other side. These detector arrays were interleaved with the layers of steel absorber. Each Iarocci tube had eight 9 mm $\times$ 9 mm $\times$ 150 cm long active volumes with an anode wire at

the center of each. These sections were separated one from another by 1 mm thick plastic septa. The tubes were packaged in frames that held the readout strips in position. The readout strips were 4 cm wide for both the x and the y-strips and extended the length of the Iarocci tube array. The entire assembly was supported on a large stand used for RD10. Ten 0.5 inch steel plates were stacked together to form layers approximately 12.7 cm thick. The entire assembly corresponded to 7.5 hadronic absorption lengths. Simulation studies with GEANT indicate that a uniform spacing of steel provides good μ/π discrimination. We studied other arrangements with increasing or decreasing thicknesses of steel per layer as a function of muon momenta. This arrangement produced a μ/π separation of approximately 2%. These tests also provided information concerning pulse height and gain stability.

3.5 Electronics

This section will present information about the front-end electronics for both the muon tracking chambers and the muon identifier tubes. The remainder of the DAQ electronics chain is described in the CDR Update.

3.5.1 CSC Electronics

The muon tracker has approximately 46,000 channels of electronics on the cathodes and 15,000 channels of electronics on the anodes. The three coordinate readout on each cathode strip detector allows for space point reconstruction on each detector without the requirement of using additional detectors to resolve ghost hits. The anode electronics requirements are somewhat straight forward because no amplitude or timing information is required. The cathode, however, has somewhat more stringent requirements because the resolution achievable depends on the noise levels and the linearity of each channel.

Characteristic Counting Rates and Times

To properly design the front end electronics an understanding of the strip counting rates is needed. The updated CDR lists the following parameters,

beam condition	Interaction Rate	dN/dη	time
$p + p$	454 kHz	2.6	2.2us
$Au + Au$ (MB)	13.9 kHz	210	72.2us
$Au + Au$ (Cn)	1.4 kHz	878	721.6us

The multiplicity's quoted are from the target. Simulations have shown that the multiplicity in the muon tracker is about 50 for Au + Au central events. This means that only 0.045 of all tracks enter the tracker. This reduction factor could be applied to the MB events for Au + Au or $p + p$. The occupancies for each strip can be determined in the following manner,

Readout pitch = 1 cm
number of readouts = 6.28 × R (R = outer radius of station)
occupancy =3x (50/6.28 × R)

where 3x includes charge sharing on more than one strip. Therefore, for station 1 the strip occupancy is,

$Au + Au$ (Cn) occupancy = 0.135 counts/strip/crossing event
$Au + Au$ (MB)occupancy = 0.03 counts/strip/crossing event

The ability of the detector design to resolve all ghost hits allows us also to always know that a multiple track on the high resolution cathode has occurred. If we know that a multiple track has occurred, than resolving the two tracks is possible. The only requirement is that

the charge from both tracks be integrated correctly. This requirement implies that the integration time of the front end amplifier should be much longer than the drift time in the chamber gas so that variations in charge integration between the two tracks is minimized. Integration times of up to 500 ns are therefore desirable.

Another important parameter is the length of time available on average before unacceptable pileup occurs. If a front end shaper is used than the signal decay time can be adjusted to decay to a prescribed level so the probability of pileup is small. The average count rate is calculated as follows,

$$Au + Au \ (\text{Cn}) = 0.135 \times 1.4 \ \text{kHz} = 189 \ \text{counts/s}$$
$$Au + Au \ (\text{MB}) = 0.03 \times 13.9 \ \text{kHz} = 417 \ \text{counts/s}$$
$$\text{Total} = 606 \ \text{counts/s}$$

Given a strip rate of 840 counts/s, the probability of 2 events occurring in 100 us is 0.002, very small. Therefore, a pulse with a long tail can persist for 100 us. The decay time allowed for a pulse to decay to less than 1 bit out of 12 bits is 12 us. The specification for signal processing using a shaper is that the rise time should be greater than 500 ns and the decay time should be less than 12 us.

CSC Detector Characteristics

The cathodes have 0.5 cm wide strips and a readout pitch at 1 cm, i.e. every other cathode is readout. The intermediate cathode signal is capacitively coupled to the readout strips and the intermediate cathode will have a large value resistor of approximately 0.5 megohm to ground to prevent the strip from floating up to high voltage. The cathode strip will be copper with a resistance of approximately 1 ohm per square. The capacitance of the strip is dominated by the interstrip capacitance and is approximately 1.3 pf/cm. The amplifier will see two capacitances in series and so will see one half of 1.3 pf/cm or 0.65 pf/cm. For chambers 3 m long, the maximum capacitance for the front end electronics is 150 pf. Since the strips on all stations will be variable in length, the front end capacitance will vary from 0 to 150 pf. The high resolution cathodes will be DC coupled into the amplifiers.

The low resolution cathodes will be 1 cm strips and readout at a 2 cm pitch. The strip resistance and capacitance will be 1 ohm per square and 0.65 pf/cm respectively. The strip capacitance will vary from 0 to 150 pf. The low resolution cathode will be DC coupled into the amplifiers.

The anodes are spaced at 1 cm and will be read out at 1 or 2 cm intervals depending on the occupancy. The anodes will be at high voltage, 2500 volts, and therefore the anode signals will be AC coupled to the amplifier via a 100 pf capacitor. We expect to use a fast gas and have a maximum drift time in the gas to the anode of about 50 ns.

The Detector Signals and Noise

The front end electronics on the cathode should be designed for 80 fC or less input signal. To achieve a resolution of 100 μm due to electronic noise the signal-to-noise must be less

than,

$$S/N = \frac{\sigma}{1.65w} \tag{3.2}$$

where σ is the chamber resolution = 100 μm and w is the strip pitch = 1 cm. The required noise level is 0.6% or 0.5 fC. This is equivalent to 3000 electrons of noise.

Electronic Design Issues

The primary design issue for the front-end electronics is to maintain a signal-to-noise of better than 100/1 in the face of a large detector capacitance. For the CSC chambers, the dominant contribution to the capacitance seen by the preamplifiers is the strip-to-strip capacitance. The capacitance between adjacent strips having a thickness, t, width, w, and separation, s, laying on a dielectric with constant, k, is approximately given by,

$$C(\frac{pf}{cm}) = \frac{0.12t}{w} + 0.09(1+k)\log_{10}(1 + \frac{2w}{s} + \frac{w^2}{s^2}) \tag{3.3}$$

The second term dominates. Using k=3.5 (kapton), w=10 mm, s = 0.5 mm, t=2 μm, the capacitance is 1.1 pf/cm. For the prototype test chamber, the capacitance was measured to be 1.33 pf/cm, in close agreement to the calculated value. We expect the maximum capacitance will be less than 500 pf for all stations so a basic requirement of the front-end electronics is that it must perform to specifications with an input capacitance of 500 pf or less.

An additional concern is the coupling of the signals between adjacent strips. A test of this effect was modeled in the electronic code PSPICE for representative chamber parameters. For this simulation the strips were considered as lumped RC delay lines. The results of the simulation are shown in Figure 3.33. A current pulse similar to signals observed on the prototype chamber was injected into one end of the simulated cathode strip and the pulse response was observed at the far end of the active strip as well as the adjacent strip. The total interstrip capacitance was 300 pf, the resistance was 20 ohms, and the capacitance to the anode plane was 10 pf. The results show significant coupling to the adjacent strip and dispersion of the initial signal. However, if the signal is integrated for > 100 ns the full signal charge is preserved and the signal on the adjacent strip integrates to zero. This implies that the integration time of the electronics should be greater than 100 ns if we want to be insensitive to any distortions in the apparent induced charge distribution due to coupling from one strip to another.

Dynamic Range

The dynamic range of the high resolution cathode electronics depends on the signal to noise level, energy loss fluctuations, and a margin of error required to take into account the variations in the gain of the front end amplifiers and the following AMUs. The dynamic range is calculated as follows,

$\times$ 100 signal to noise
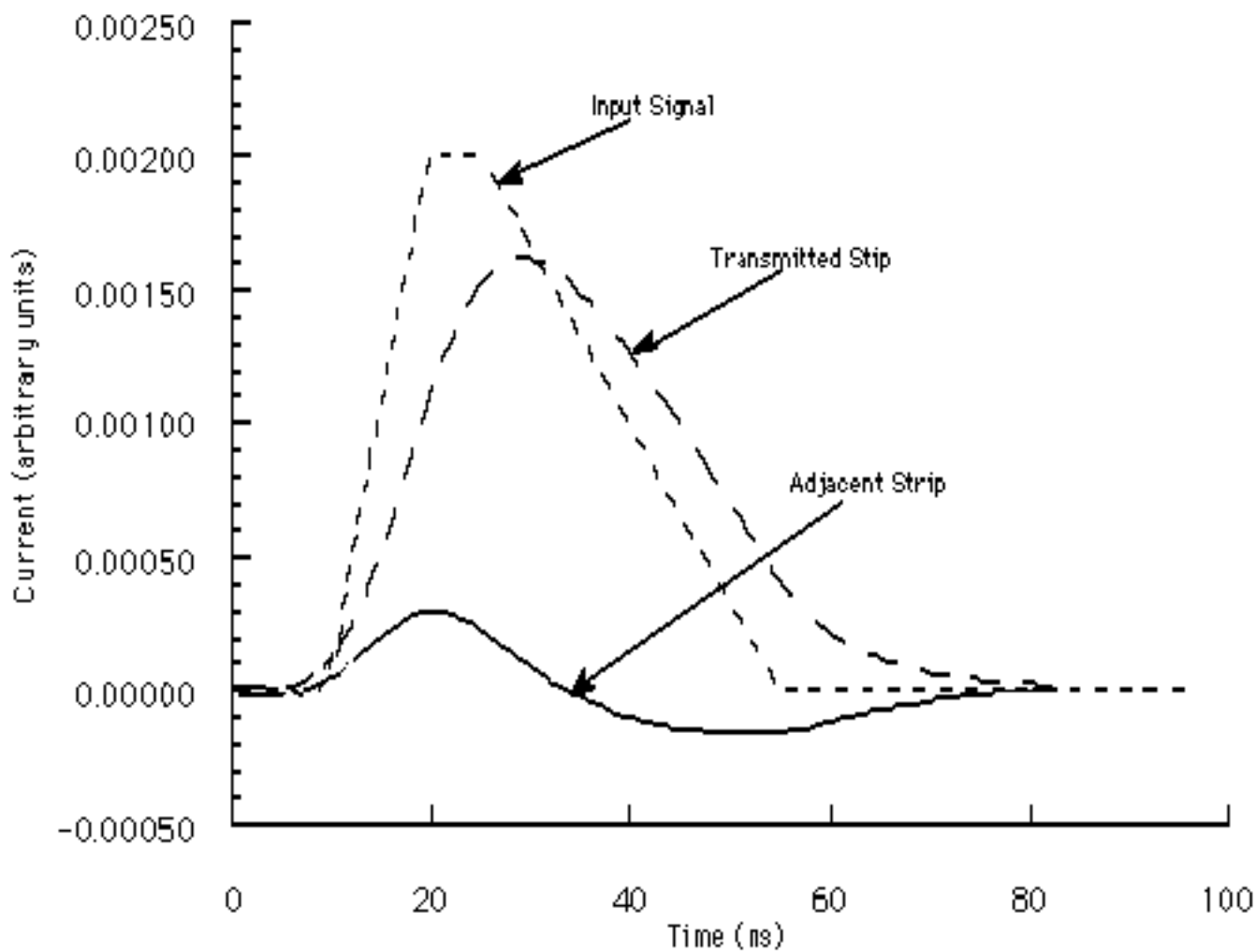
Figure 3.33: SPICE simulations of cathode strip

$\times$ 10   energy loss fluctuations
$\times$ 2   margin
2000   minimum needed dynamic range or 11 bits

Our amplifier and AMUADC design that is to be used on the cathodes has a dynamic range of 11 bits.

The Anode Front End Electronics

The signal to noise requirement for the anode and cathode front ends are simply that the noise level should be low enough so that at a thresold adjusted to give >99% efficiency, the noise contribution to the strip or wire singles rate should not be significantly greater than the singles rate with beam. The threshold should be a factor of three below the most probable

signal. The threshold to noise is determined from the following,

$$\frac{V_t}{\nu} = \sqrt{-2\ln(4\sqrt{3}f_n\tau)} \tag{3.4}$$

where V_t is the voltage threshold, ν is the noise level, f_n is the noise frequency, and τ is the amplifier time constant. For a time constant of 500 ns and a noise frequency of 85 counts/sec, the threshold to noise should be 4/1. If the signal to threshold is 3/1 than the signal to noise should be 12/1.

The CSC anode front end can be identical to the front end being designed for the Muon ID. That is now the baseline design.

3.5.2 Muon Identifier Electronics

We will operate the LSTs in proportional mode to ensure maximum longevity. To ensure adequate signal-to-noise performance in the unknown noise environment at RHIC we settled on a readout scheme that employs in-panel amplification (x100) driving differential signals on twisted-pair cables that are long enough (20m) to reach a crate-based processing system which must discriminate the signals, provide variable delay so that all signals from a beam crossing lie within a single beam clock cycle and pass them to the LVL1 trigger and the data acquisition system. A block diagram of the readout scheme at this broad level is shown in figure 3.34 below.

In-panel Amplifiers/HV Distribution Boards The primary requirements on the in-panel portion of the electronics were longevity (anything inside a panel is inaccessible for the lifetime of the detector) and a very aggressive schedule (the decision to go with an in-panel amplification scheme was taken in 3/97 and the first boards were required for installation into panels by 10/97).

A MUID readout channel consists of the anode output of the two staggered LSTs that comprise a 2-pack. The passive OR of these (negative-going) signals is capacitively coupled into the amplifier circuit. By performing this OR immediately at the tube endcap we halve the number of readout channels (6340 total). Depending on the final concentration of isobutane in the gas mixture the most probable input signal size is between 75 and 150 pC. The amplifier gives a MIP signal heights of 150-300 mV (both sides, differential) after 20m of twisted-pair cable.

In addition to signal amplification the in-panel portion of the electronics must distribute high voltage to the LSTs.

The final scheme has 6 readout channels mounted on a $8.2 \times 50.4\,\text{cm}^2$ printed circuit board. Different channels share power buses (+/- 12V), a pulser circuit, HV buses (separate buses for the two LSTs in different planes serviced by each readout channel) and a ground plane. The amplification circuit and HV distribution circuit are mounted on opposite sides of the board so that the HV can be isolated from human contact during panel assembly. Each channel is identical and sits in an 8.4 cm (the width of one LST) wide section of the board. The number of channels per board was determined by the largest board that could be produced in a standard press. The boards are mounted inside the panels at the LST endcaps and connected to the LSTs with custom HV connectors. See figure 3.35 below.

To speed development the amplification circuit was largely borrowed from an L3 design. The circuit diagram is shown in figure 3.36 below. Several features were incorporated to improve longevity:

1. The power inputs for each channel have resettable polyfuses so that a short on one channel will only affect that channel.

2. A double diode protection circuit was found to be necessary to allow an amplifier channel to survive the spark created when a wire breaks while under high voltage. With this feature a readout channel can continue to operate at high efficiency even after one of its input LSTs has died.

MuID Data Flow

Readout Card

LEMO Front-Panel Testpoints

Analog spy MUX

Digital spy MUX

Panel

Two-pack

Preamp

Buffering for LVL1 latency
and 5-event storage

Variable Delay

LED

Differential Receiver

G-link to DCM
via backplane, FEM

20 m twisted-pair

Front panel G-link to LVL1
MUX @ 6*BMCLK
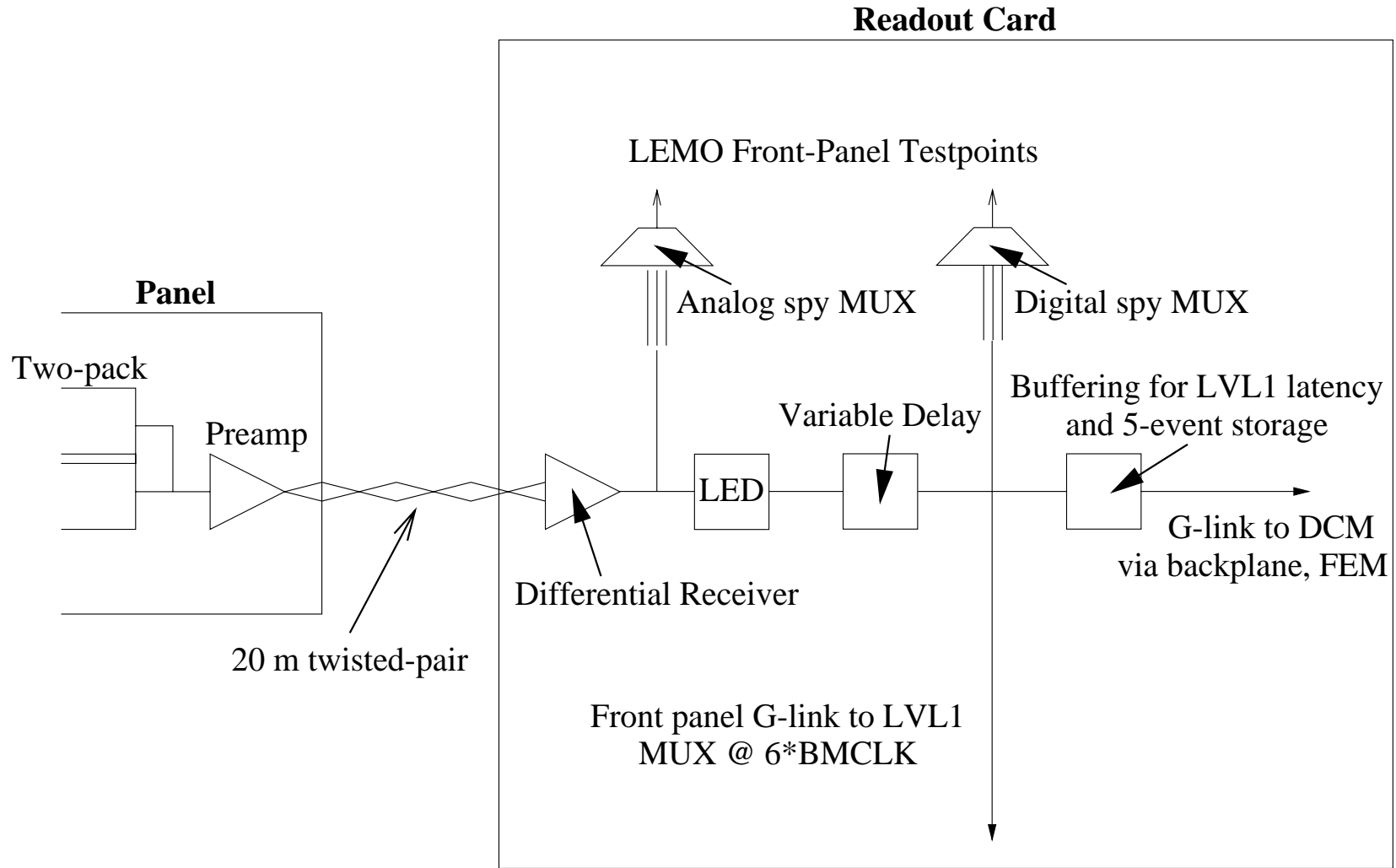
Figure 3.34: Block diagram of MUID FEE readout scheme.
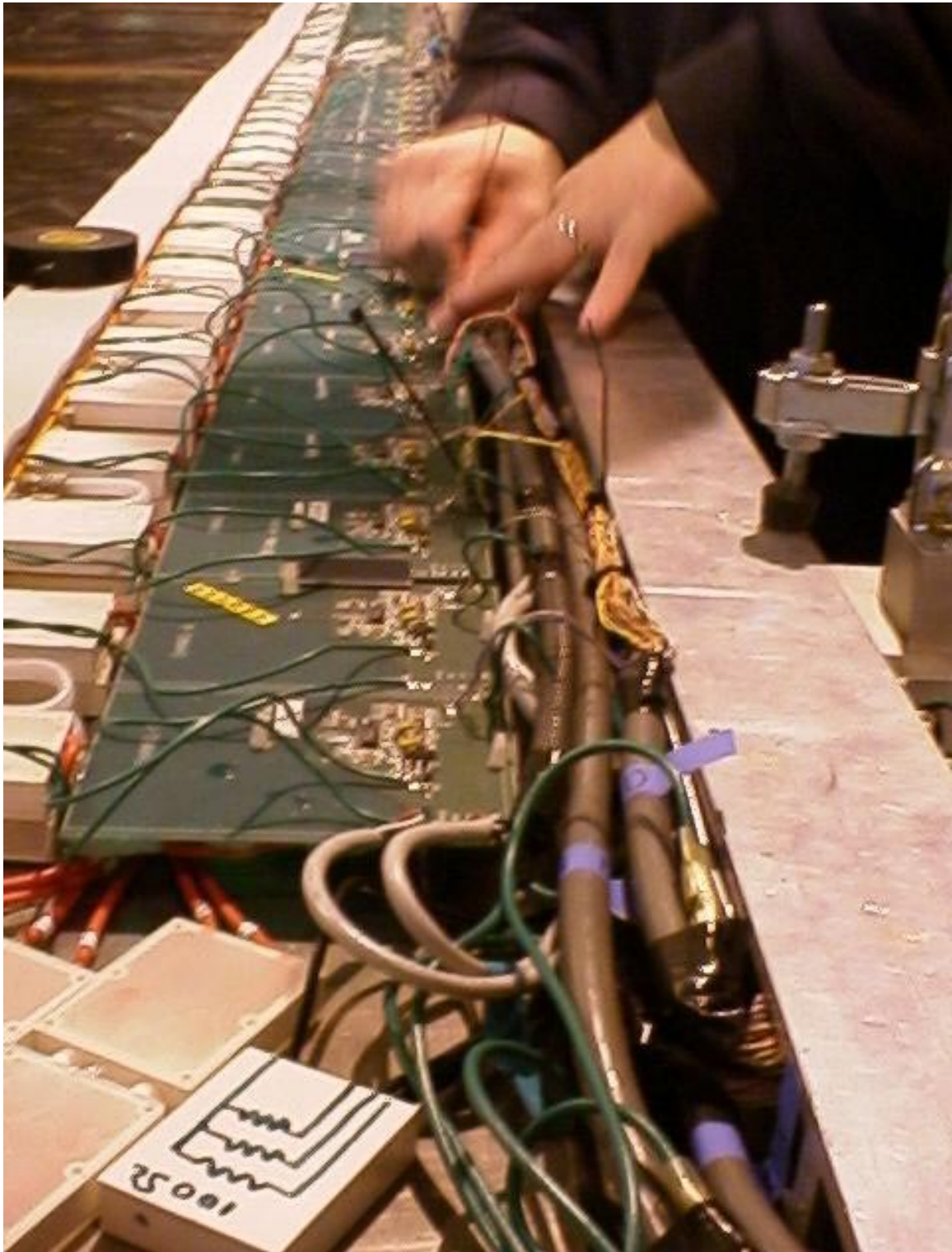
Figure 3.35: View of in-panel amplifier/HV distribution boards installed in the first production MUID panel.

3. Diode clamps were added to prevent reverse-bias damage.

In addition there is overload circuitry added to set a saturation limit for very large signals and the output stage was changed to be *pnp* to reduce quiescent power consumption while maintaining dynamic range.

The HV circuit complies with Mil. Spec. 275D (which specifies 0.00012"/V separation on a printed circuit board) at 5000V. The HV input for each LST has a $400\,M\Omega$ current-limiting resistor so that the HV for the circuit will continue to operate with multiple tube failures (seven or less failures with $I_{max} = 100\,\mu A$). All components under HV are encapsulated in a silicone conformal coating to enhance longevity and safety.

In addition to these steps, we have maintained a design in which different LST planes are on independent separate gas and HV circuits and each plane is further segregated into roughly 24-channel HV, gas and power segments.

Out-panel Electronics   The system design for the out-panel (post-amplifier) elecronics has reached a relatively mature state and prototypes of some components have arrived.

We are using a crate-based architecture (VME 9U). Each crate has three types of cards referred to as Front End Modules (FEMs, 1 per crate), Readout Cards (ROCs, 20 per crate) and transition cards (TCs, 20 per crate). In addition, there are two custom backplanes. One is simply passthrough pins to bring signals into the ROCs from the TCs. The other is the ROC/FEM communication bus. The FEM in each crate communicates with its own DCM, timing/control module and ARCNet node. Front and side views of the crate concept are shown in figures 3.37 and 3.38 below. Various considerations led us to a 96-channel ROC, which results in four crates for the entire MUID; one each for North Arm Horizontal tubes, North Arm Vertical tubes, South Arm Horizontal tubes and South Arm Vertical tubes.

Simulations have determined that only the discriminated output of each channel (the struck 2-pack bit pattern) is needed to give the required pion rejection. Therefore the MUID data consists of 96-bits per ROC (1920 bits per crate). The same data is sent to both the DCM and the LVL1 trigger.

Transition Cards/Passthrough Backplane   Signals enter the TCs from the back on six 17-pair twisted cables (16 data pairs and one ground pair). They are brought into the ROCs through a backplane that simply consists of passthrough pins. This eases maintenance by allowing the insertion/removal of a ROC without removing the signal cables. The six input connectors are 34-pin IDC. In order to get the signals into the ROCs in the required 6U height (to allow 3U for the ROC/FEM communication bus) the two passthrough connectors are 160-pin DIN. A picture of the prototype TC is shown in figure 3.39 below.

Front End Modules (FEMs)   The FEM cards are analagous to a conventional crate controller, providing the interfaces between the MUID and the PHENIX online systems (with the exception of LVL1):

1. The ARCNet interface receives the serial control commands, translates them into lower-level instructions that are routed by geographical addressing on the backplane and
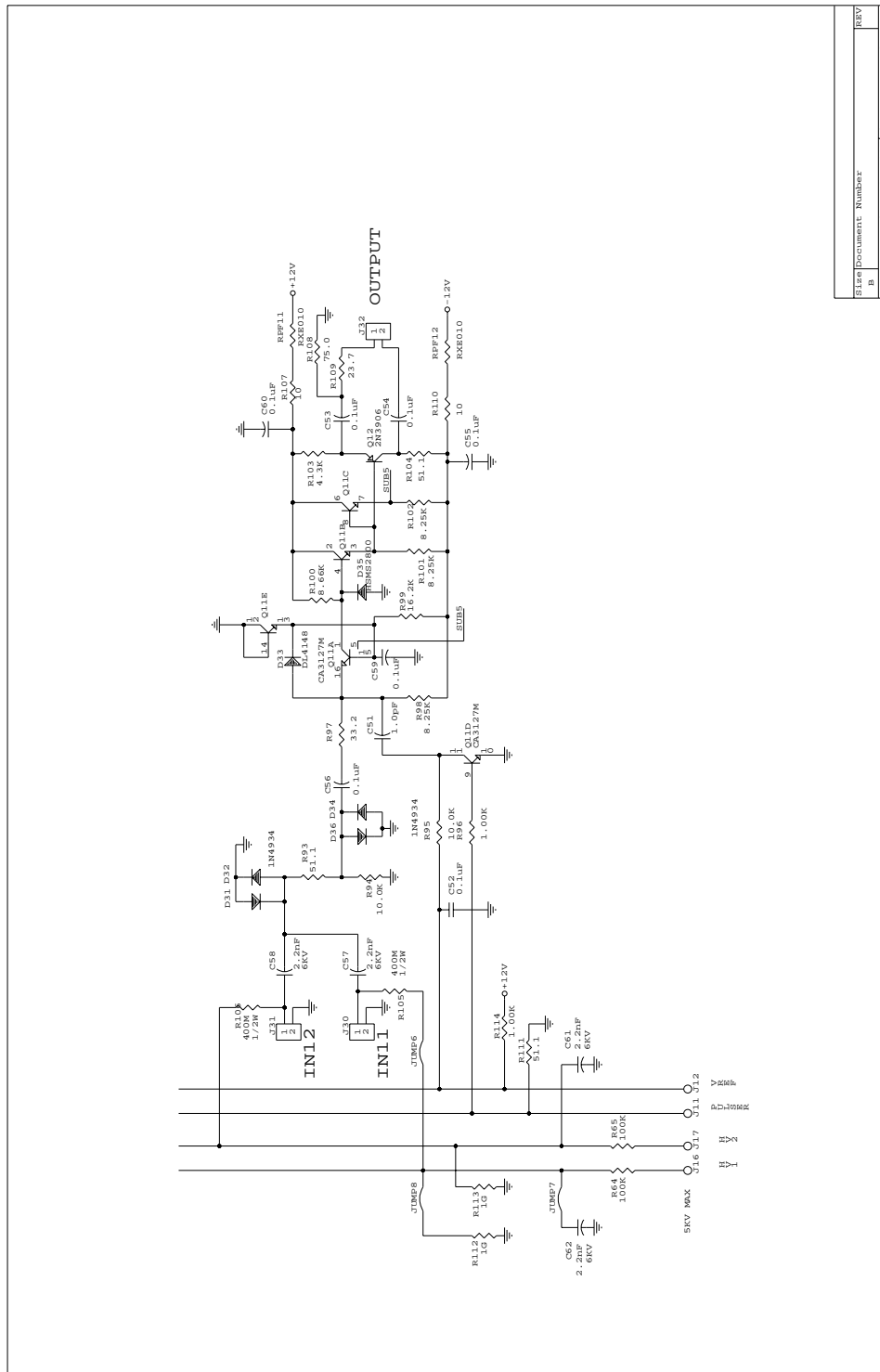
Figure 3.36: In-panel amplifier/HV distribution circuit diagram.

Front of FEM Crate
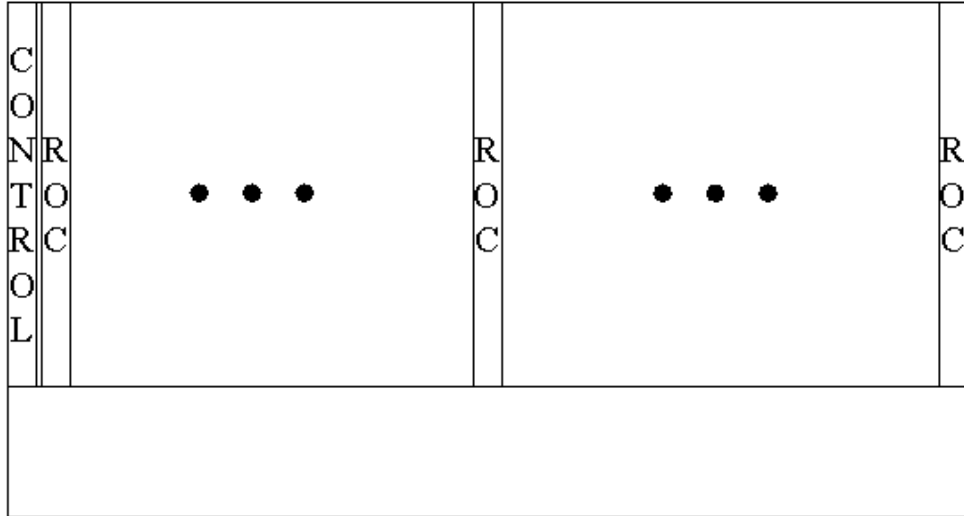
Figure 3.37: Front view of the crate concept.

CPLDs on each card and allows readback of the programmed state. Cards can be addressed individually and through a broadcast mode.

2. The timing and control interface receives mode bit information and uses a state machine to parse the instructions, validate them and route them to the appropriate places.

3. The DCM (data output) interface assembles and ships out the data packet for each event. A state machine cycles through all ROCs in the crate, copies their data (struck 2-pack bit pattern) into a DCM FIFO and builds header/trailer words.

The FEMs have an FPGA that allows them to be exercised in the absence of a ROC. This FPGA consists of a block of RAM (programmable via serial control) and spy lines to the data bus. When the self-test mode is selected the FPGA is read instead of the ROCs.
The block diagram of a FEM is shown in figure 3.40 below.

ROC/FEM Digital Communication Backplane   One 3U backplane in each crate provides power and digital communication between the ROCs and the FEM. This backplane

FEM Crate Profile
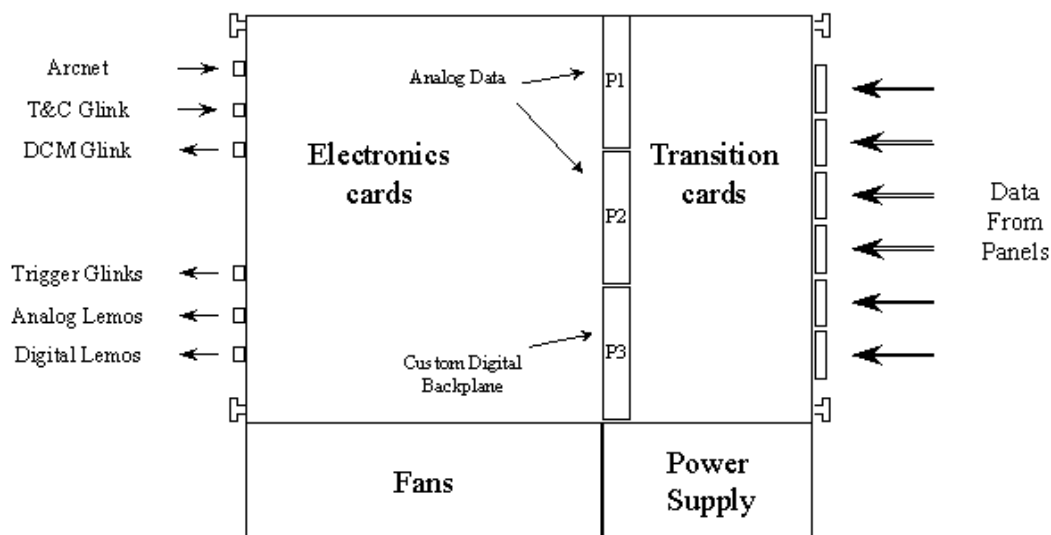
Figure 3.38: Side view of the crate concept.

is modeled after the VME64X backplane (geographical addressing, 10 MHz communication, termination) but has been customized to optimize pin placement and analog power/ground referencing.

Readout Cards (ROCs) The ROCs can be broken into the analog processing chain, supplemental diagnostics and serial control. The purpose of the analog processing chain is to receive the input signals, provide leading edge discrimination and variable delay and feed these digitized outputs into the LVL1 trigger and into FIFOs to match LVL1 delay and pending sample storage requirements. The diagnostics include a maskable pulser and 96-to-1 analog and digital "spy MUXes". The block diagram of a ROC is shown in figure 3.41 below.

The first stage of the analog processing chain is a differential receiver for the input signals. The CAMAC-resident receiver module used to test panels during assembly successfully used an amplification factor of 1 with a threshold of 40 mV and a 50/50 isobutane/CO_2 gas mixture (maximum gas gain). For the final electronics an amplification of 3 was chosen to optimize filtering characteristics and as a hedge against a lower gas gain that will obtain if the operational gas mixture is chosen to have less than 50% isobutane. The discriminator
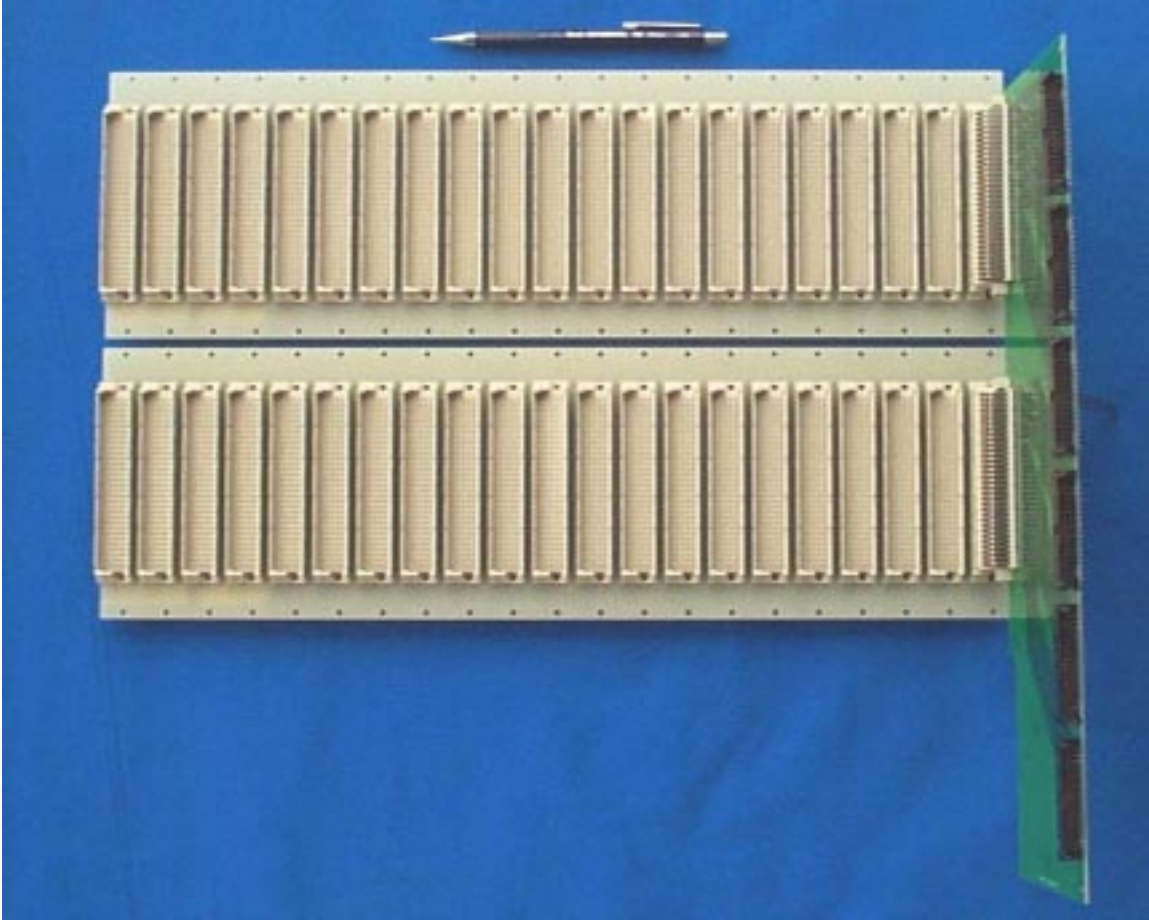
Figure 3.39: View of the transition card plugged into the passthrough backplanes.

threshold is adjustable (12.5-500 mV, 256 steps) every four channels.

Because of the pipelined, deadtimeless architecture of the PHENIX data acquisition system all signals for a LVL1 input detector must arrive within one beam clock cycle (106 ns, see figure 3.42 for explanation below). In fact, setup and hold considerations reduce the maximum gate width to roughly 90 ns and convolution with transmission down the length of the LSTs further reduces the maximum gate width to roughly 80 ns.

One obvious solution is to use a fast gas. CF4 is ideal except for its very expensive operational cost (both venting and recirculating). Another solution is the OR'd readout of staggered LSTs that we are already incorporating for geometrical efficiency and redundancy reasons - a particle will pass near an anode wire in one of the two LSTs in a 2-pack, thus minimizing the drift time for the readout channel.

For the final configuration the inefficiency as a function of gate width for a 2-pack read-out from a particular point along its length is shown in figure 3.43 below. The maximum obtainable efficiency can be read off the graph (95% at the 80 ns gate width). Failure to
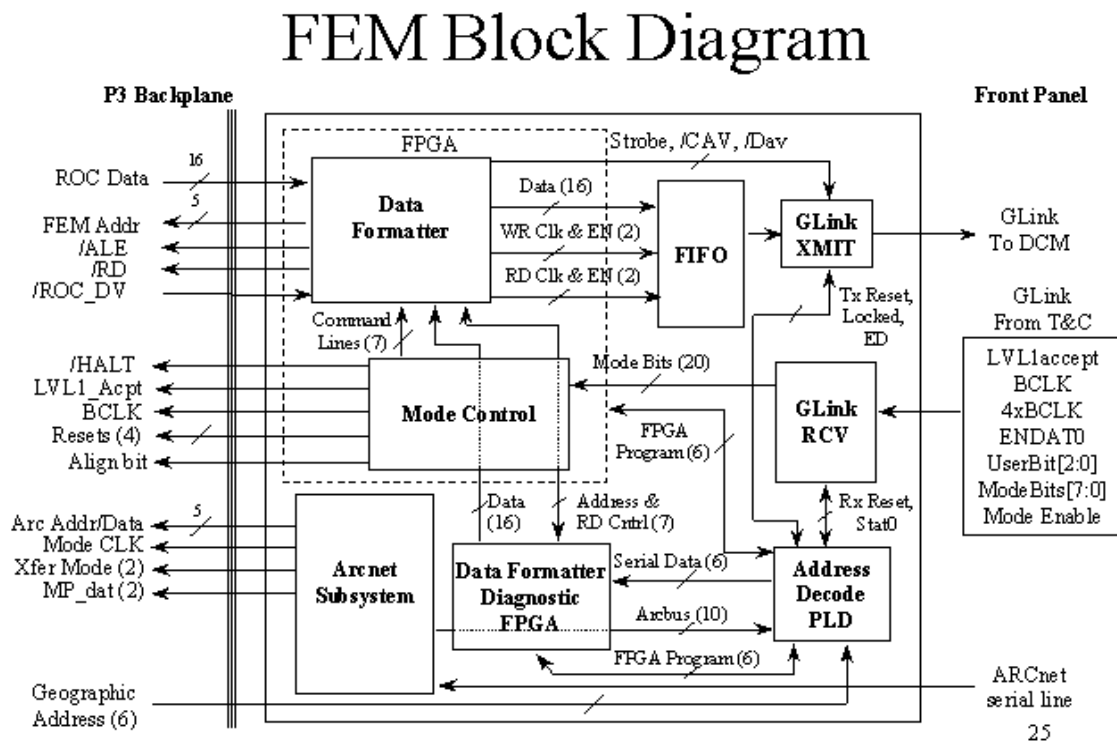
FEM Block Diagram

Figure 3.40: FEM block diagram.

equalize t_0 for each channel results in an efficiency loss of $\approx 1\%$ every 3 ns.

There are sources of t_0 skew that are common to an entire ROC, sources that are common to 16-channel groups (the 16 channels on each input cable) and sources that are unique to individual channels (see table 3.8, below).

This leads to the following specs for the variable delay:

1. Dynamic Range : 50 ns

2. Dynamic Range (w/i 16-cable bunch) : 25 ns

3. Resolution: 4 ns

4. Precision : 1 ns

Due to space, cost and implementation considerations the variable delay has been implemented in a staged fashion. All skew common to 16-channels or more is eliminated by passing the beam clock for that 16 channels through a programmable delay chip (six per board) with dynamic range and resolution to spare. Channel-to-channel skew cannot be
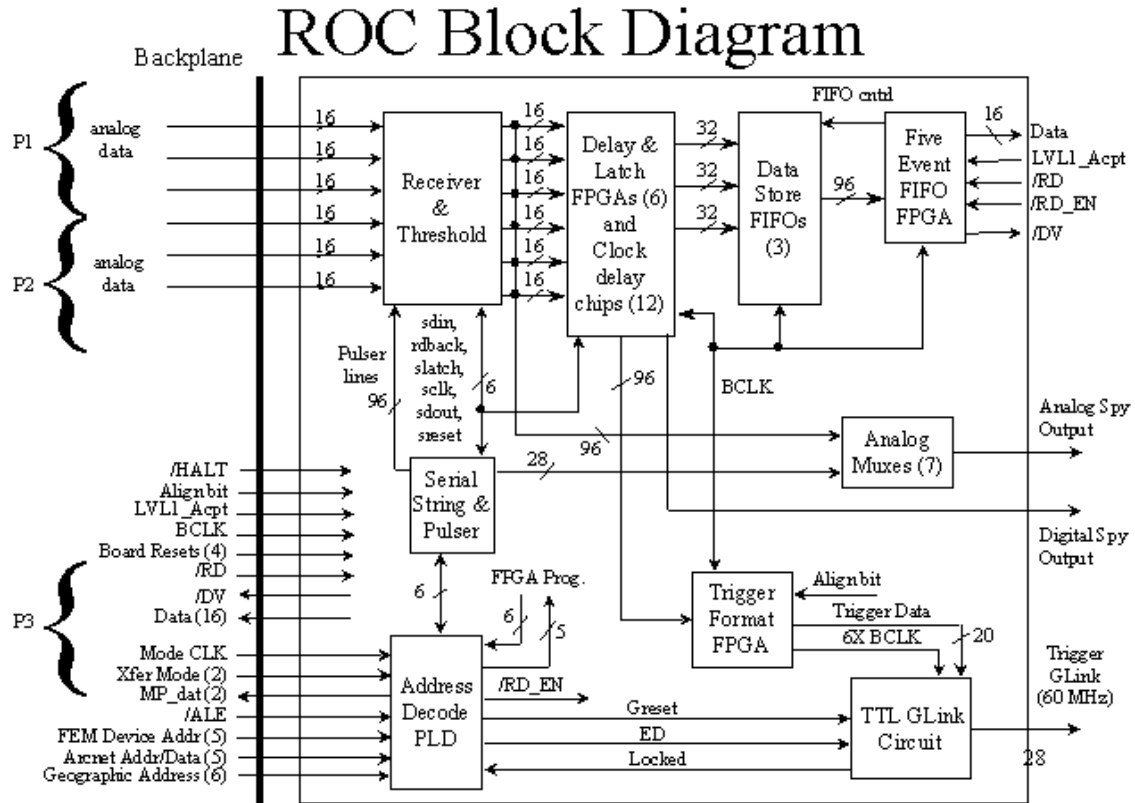
Figure 3.41: ROC block diagram.

Skew Source	Granularity	Maximum Δt
ROC/FEM Drivers	96	5
Flight time to different gaps	16	8
Different internal cable lengths	1	5
Different flight time to LSTs on a cable	1	5
Trace lengths	1	2
Insertion time differences	1	10

Table 3.8: Source, granularity and size of contributions to MUID signal skew. Any skew leads to an inefficiency ($\approx 1\%/3\,\mathrm{ns}$) because signals will fall outside the 80 ns effective gate.
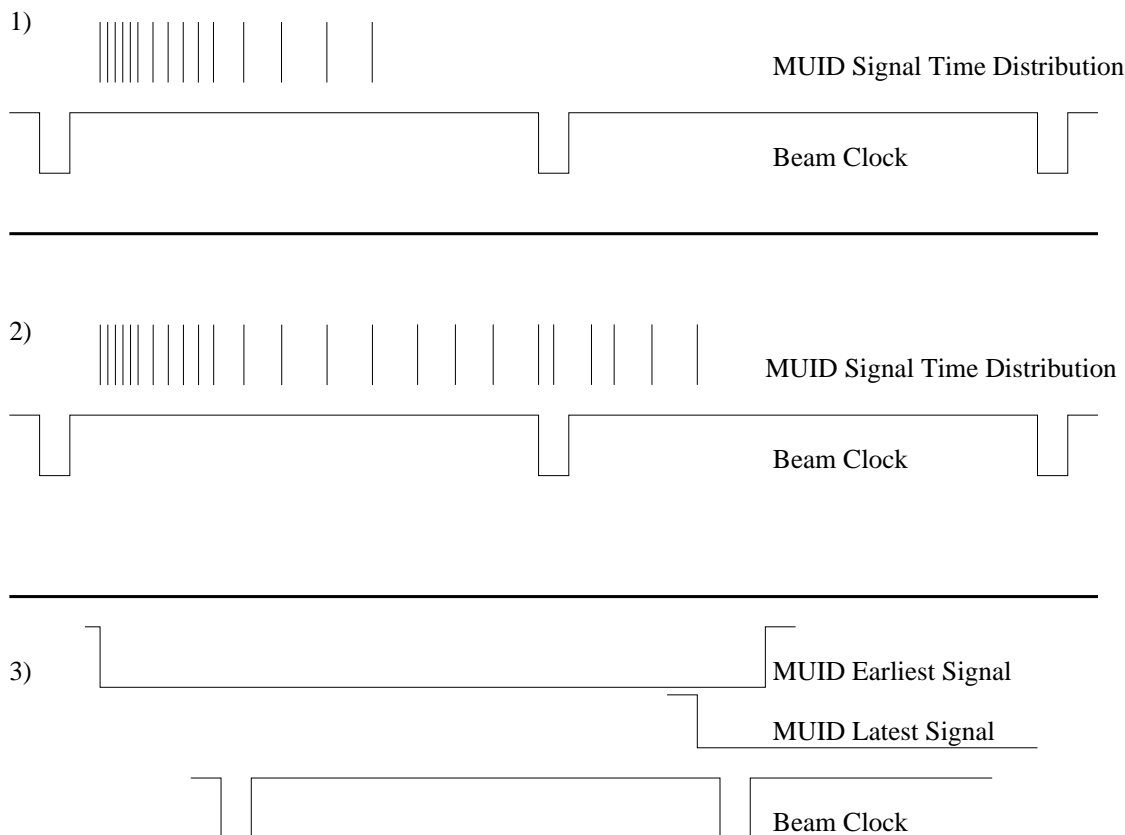
Figure 3.42: Case 1 shows an ideal situation in which all signals from the detector fall within one beam cycle. Signals are latched at the second beam pulse. Case 2 shows a situation in the signals are not all present at the second beam pulse. Latching signals at the second beam pulse results in some inefficiency. Case 3 shows the natural solution for a non-pipelined system: one would simply use the input signals to strobe a one-shot with a width longer than the largest Δt between hits in a single event. The signals get strobed in on the second beam clock shown. Unfortunately the first beam clock would also strobe in signals from this crossing, thus possibly giving a valid LVL1 trigger for the wrong event.

eliminated in this fashion because of cost and board space. Instead, individual channel skew is eliminated by passing the delayed beam clock through a multitap delay line. The different delays (0-28 ns, seven 4 ns steps) are each sent to 16 multiplexers in a CPLD: the delay for each channel is set by selecting the best input.

The data from each ROC are sent to the LVL1 trigger where a steerable road algorithm is implemented to determine if there are candidate muon tracks in the event. The 96 bits of data from each ROC are multiplexed into six 16-bit words and sent to the trigger via optical G-link connection (one per ROC) at six times the beam clock frequency.

Because of the PHENIX pipeline architecture the data from every beam crossing must be stored for a time equal to or greater than the LVL1 latency before either being formatted
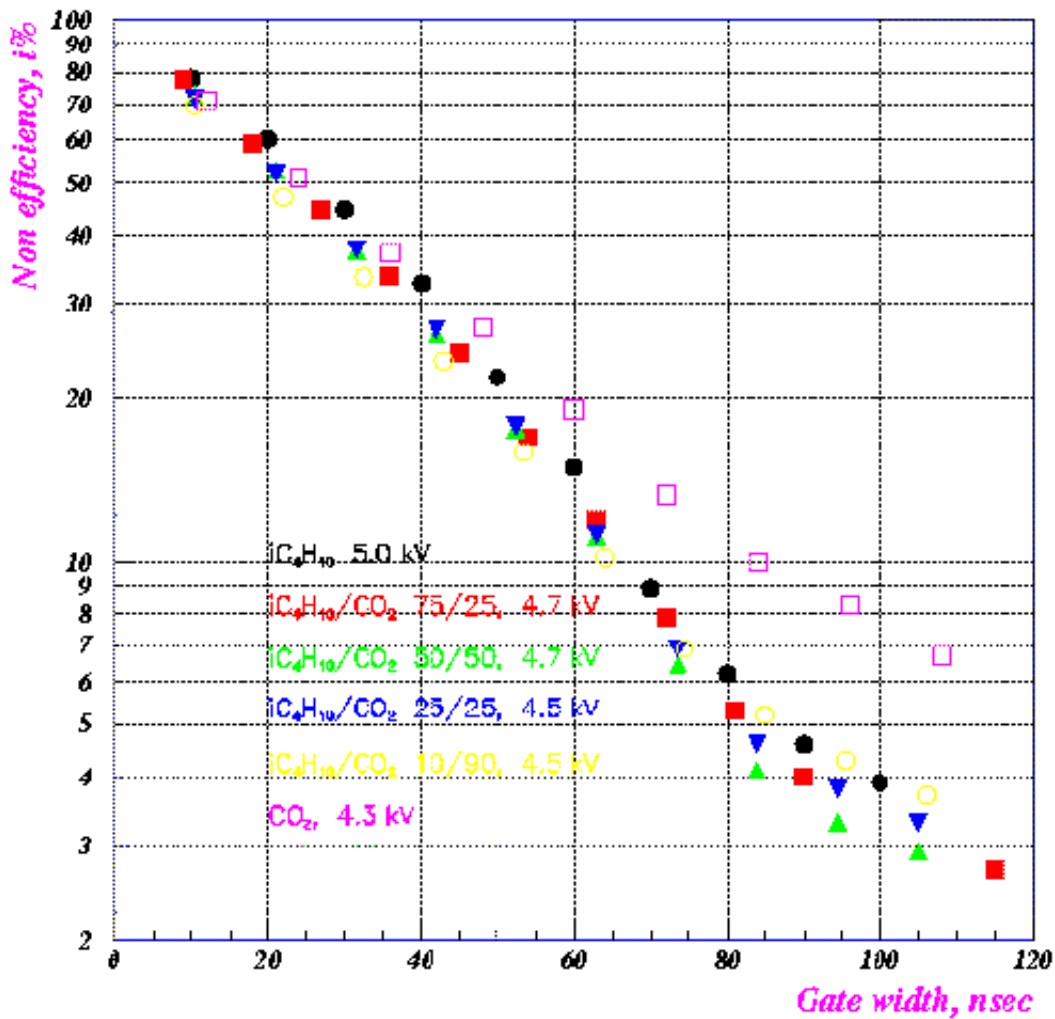
Figure 3.43: Inefficiency versus gate width for one 2-pack at a single point along its length. See color key for operational gases tested.

into a packet and shipped to a DCM or discarded (if the event did not satisfy LVL1). This is accomplished with three 32-bit 64-deep FIFOs.

If the event satisfies LVL1, the data for each ROC moves to another level of buffering that must be capable of storing five LVL1-triggered events. This is implemented as one FPGA-resident 112-bit 5-deep FIFO on each ROC. The 112 bits stored for each event include the 96 data bits for that ROC plus a 16-bit beam counter which serves as a timestamp to identify communication errors.

A pulser is implemented on every channel to allow for diagnostic tests of the board itself

and to strobe bit patterns through to test the LVL1 trigger algorithm. The pulser has a 4-channel granularity. In addition, every channel can be individually masked.

Spy lines for both analog signals (immediately after the receiver) and digital signals (after the variable delay) are sent through 96-to-1 multiplexers with output channel selectable via serial control. These "spy MUXes" drive $50\,\Omega$ output signals accessible through front-panel LEMO connectors.

The FEM/ROC serial control communication protocal contains an address word that specifies broadcast mode or the geographical address of the ROC being addressed. A second address word specifies the type of data being communicated:

1. Set/readback threshold DACs.

2. Set/readback programmable delays.

3. Set/readback selected delays.

4. Set/readback pulser selects, MUX selects, output mask selects.

5. Download FPGA programs.

An identical state machine on every ROC and FEM directs the data to the correct location.

3.5.3 Muon Identifier Trigger

MUID is an important contributor to the LVL1 trigger decision. Simulations have shown that MUID trigger algorithm needs to be capable of tracking steered one-dimensional roads through the detector and allow at least one missing gap.

The input to the algorithm is the struck bit pattern of the entire detector. The data has been arranged to simplify the MUID LVL1 hardware implementation. In particular, a given LVL1 board can only look at 5 optical fibers (25% of the data that must interact to track a particle through one arm in one orientation). So, 4 LVL1 boards must communicate through the LVL1 crate backplane (cross-stitching). To minimize cross-stitching the horizontal and vertical orientations in each gap have each been divided into 4 sections. These sections each go into a single ROC. The corresponding sections for each of the 5 gaps are communicated to a single LVL1 board via 5 optical fibers (one per ROC). This illustrated in figure 3.44 below.

A candidate local level 1 (LL1) algorithm that tracks steered roads and allows skipped gaps is shown in figure 3.45 below. Other implementations are possible and will be examined. The output of the LL1 algorithm is a set of LL1 primitives that are used by global level 1 (GL1) and a set of inputs for the level 2 trigger (LV2). The LL1 primitives, shown in table 3.9 below, are a set of 8 2-bit words that give the number and depth of roads found by the LL1 algorithm. Note that the gap corresponding to the shallow/deep seperation can be programmable. The GL1 algorithm is programmable and makes use of the LL1 primitives. For instance, it can be programmed to select events with any combination of
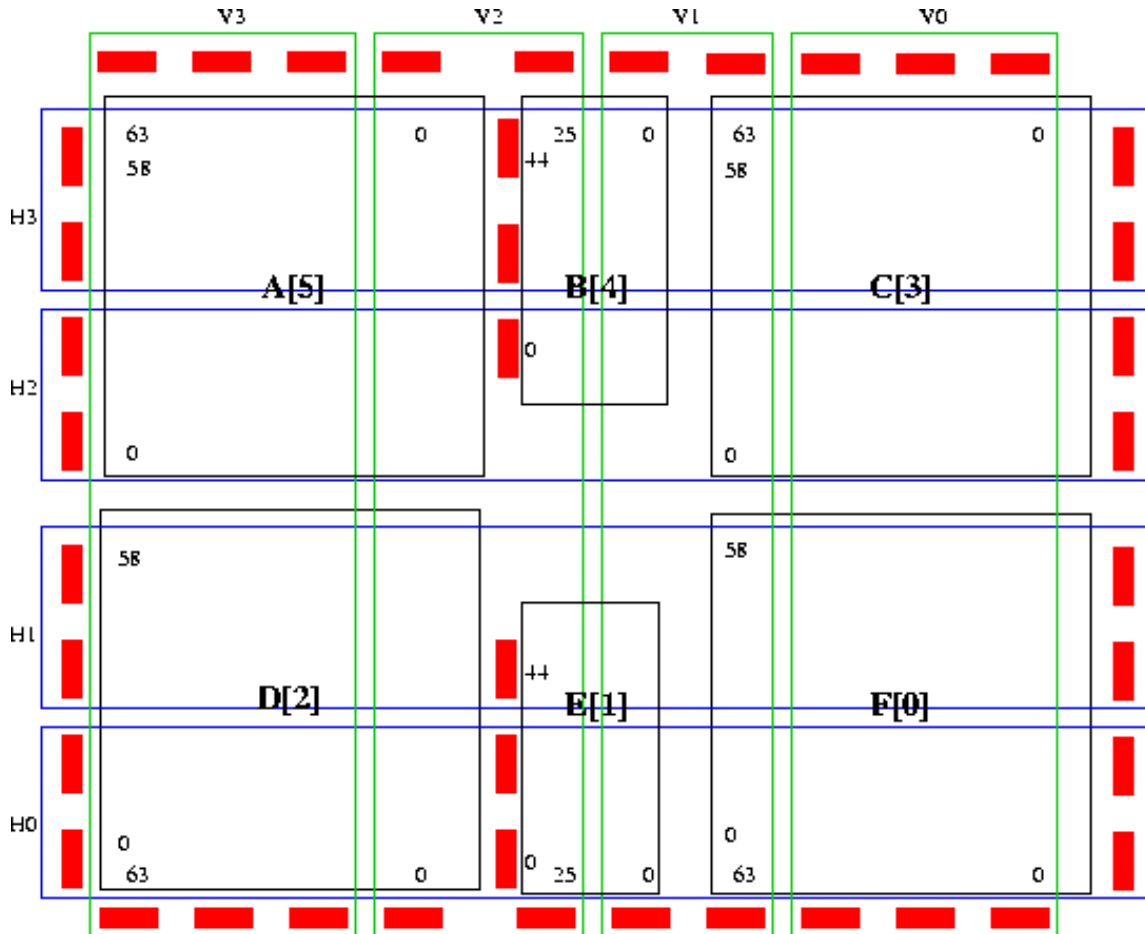
Figure 3.44: The red boxes are the 16-channel cables that are used to read out the panels. The blue and green open boxes correspond to cable groupings going into 96-channel ROCs. The 8 ROCs per gap are labeled H0-3 and V0-3. The matching ROCs from each gap in an arm (e.g., H0 from gaps North 1-5) go into a single LL1 "Board 1". These are labeled Board-1:NV0, Board-1:NV1, etc.). There are thus a total of 16 Board 1's for the entire MuID.

the LL1 primitives; e.g., 1 shallow north x-road *and* 1 shallow north y-road. The muon LV2 trigger will combine the roads found for MUID in LL1 with information from the muon tracker to form a more selective trigger criteria. The MUID LV2 inputs, shown in table 3.10 below, are 2-bit words for every 2-pack in the first gap that tell how deep a road starting on that 2-pack penetrated into the MUID.
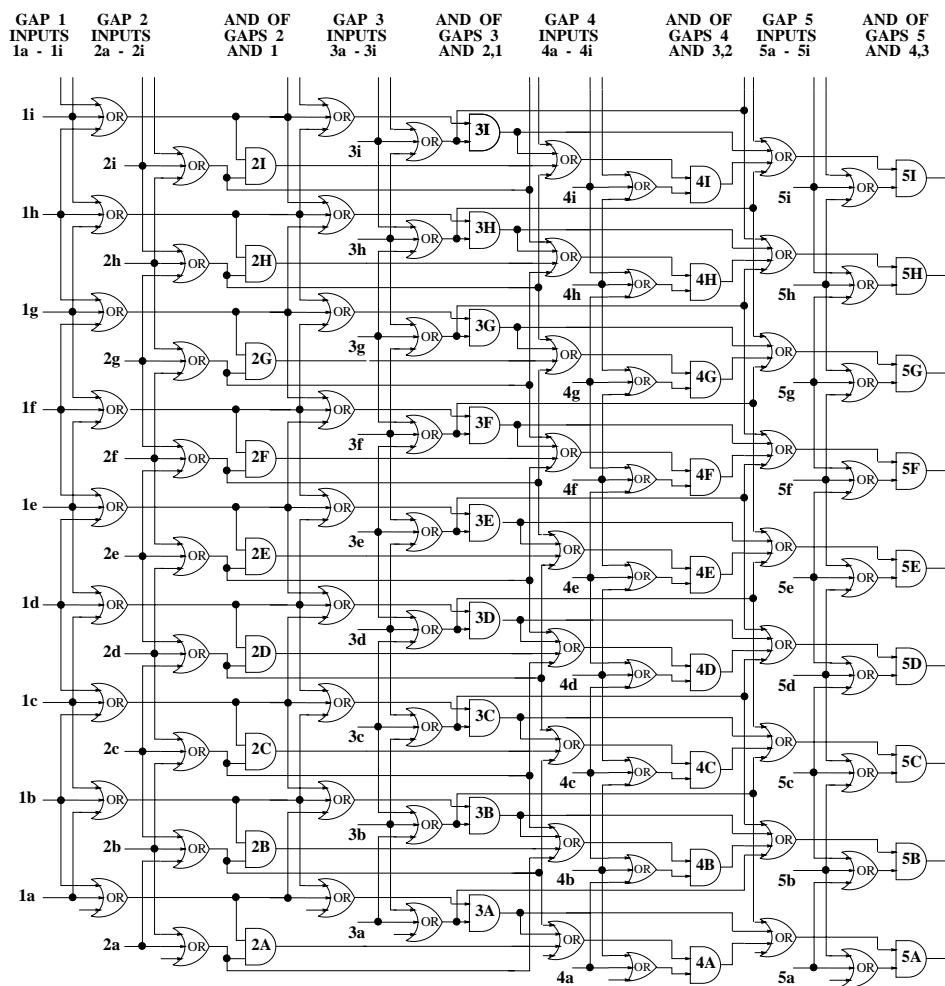
Figure 3.45: Candidate MUID LL1 algorithm hardware implementation.

N_NXS	Number of North, shallow, X-roads
N_NYS	Number of North, shallow, Y-roads
N_SXS	Number of South, shallow, X-roads
N_SYS	Number of South, shallow, Y-roads
N_NXD	Number of North, deep, X-roads
N_NYD	Number of North, deep, Y-roads
N_SXD	Number of South, deep, X-roads
N_SYD	Number of South, deep, Y-roads

Table 3.9: MUID LL1 primitives.

LV2 input binary value	Meaning
00	No road
01	Road through gap 3
10	Road through gap 4
11	Road through gap 5

Table 3.10: MUID LV2 inputs.

3.6   CSC Gas System

The gas system for the Cathode Strip tracking chambers will be a closed gas recirculating system designed to maintain the purity while at the same time conserving gas and preventing release to the environment. Because of the small Lorentz angle, Carbon Tetrafluoride (CF_4, or freon-14) was chosen, in a 50:50 mixture with isobutane [$CH(CH_3)_3$]. While a system in which the chamber gas is vented into the atmosphere would be much simpler, there are two primary reasons to use a recirculating system over venting the gas:

Environmental: Venting the gas would release 4.8×10^3 m^3/year of CF_4 into the atmosphere and an equivalent amount of Isobutane at the desired flow rates. CF_4 is a refrigerant gas whose release may be regulated in the future.

Cost: CF_4 is an expensive gas. At 9 gas volume changes per day, venting the CF_4 to the atmosphere would cost \$780,000 per year.

Specifications and Requirements

The recirculating system must meet the following requirements:

Flow rate: The system must be capable of 9 gas volume changes per day. This number was found to be adequate in tests. Table 3.11 gives station volumes and flow rates for 10 changes per day. The gas flow must be measured both entering and exiting the chambers to assure that the desired flow rate is maintained.

Overpressure: The gas pressure across the windows of the chambers to the atmosphere should be less than 2 Torr.

Gas Purity: Over time, air may diffuse into the system. The system must monitor and control the purity of the recirculating gases by removing any air which may have entered the system.

Table 3.11: Volume and flow rates of gas into each tracking station assuming 10 exchanges per day

Station	Volume (liters)	Flow Rate (liters/min)
1	120	0.83
2	630	4.38
3	710	4.93
Each Arm	1460	10.14
Total	2920	20.28
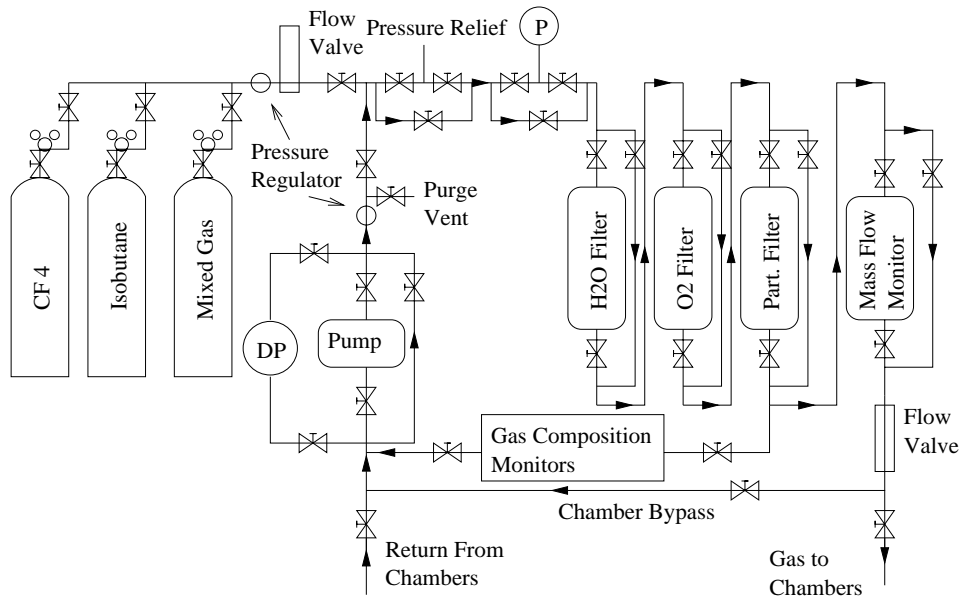
Figure 3.46: Prototype Gas System

Safety: Isobutane when mixed with sufficient air is a flammable gas. Any leaks in the system must be readily detectable.

A prototype gas system similar to PHENIX muon needs was designed for the GEM central tracker and can be modified for use with the CSC's. Based on this system, a preliminary design for the CSC system has been made and is shown in Figures 3.46 and 3.47.

The system is designed so that most parts and sensors can be located far from PHENIX so inspection and repair can be enabled during accelerator running. This includes all items shown in Figure 3.46. The combination of the pumps and a pressure regulating valve controls the flow entering and emerging from the chambers. Filters will be used to remove impurities from the recirculating gas, and gas composition analyzers will monitor the levels of O_2 and H_2O in the system. The relative concentrations of isobutane and CF_4 will be monitored using a Thermal Conductivity Analyzer.

The concentration of isobutane in the gas mixture is not flammable, since there is not enough oxygen present for it to ignite. However, a leak which allows the gas to mix with air will easily produce a flammable mixture. The leaks of the gas will be detected in several ways. First, naturally, flammable gas detectors will be installed in several locations, including near the gas recirculation system, near the manifolds which split the gas flow to the stations and octants and within the magnet near the stations themselves. Additionally, leaks will be quickly noticed by (1) mass flow meters on input and exit of chambers, (2) pressure sensors on the chambers and (3) impurities in the recirculating gas—monitored at the ppm level.

The chambers are protected from both overpressure and underpressure by use of a bubbler which allows gas to bypass the chambers if there is too much pressure at the input or to little pressure at their output. Additionally, there are gas bladder bags at the outputs of the chambers which will inflate and deflate with changes in atmospheric pressure.
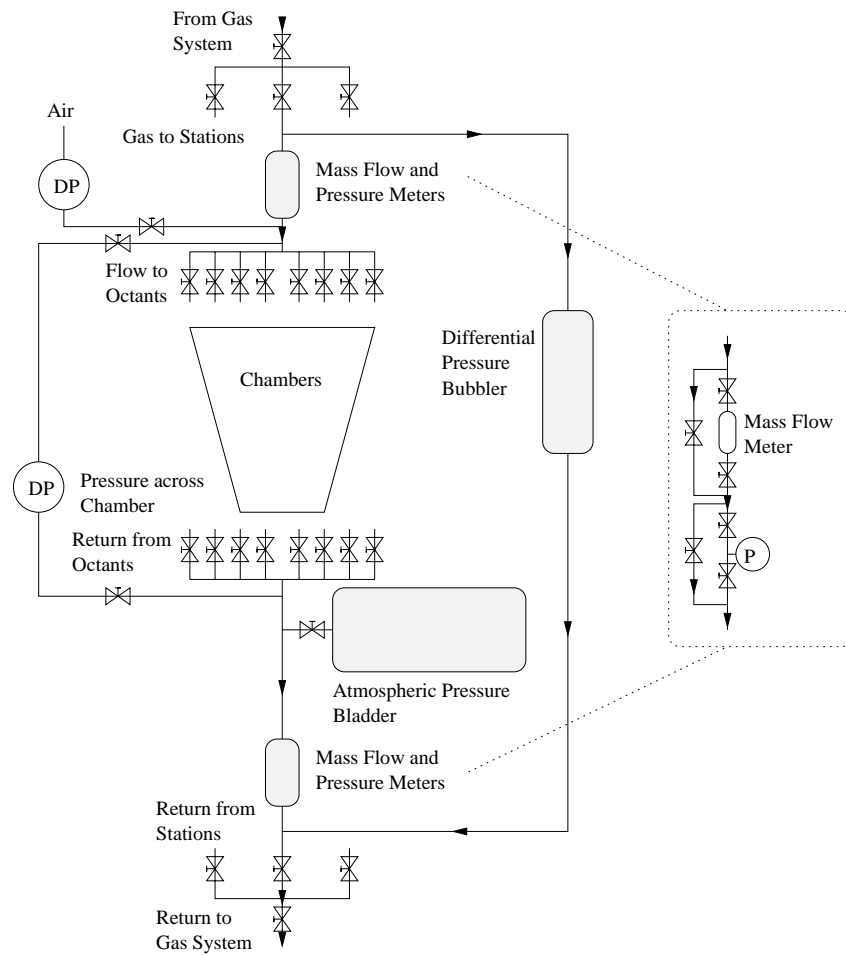
Figure 3.47: Prototype Gas System